Kinetic study and deactivation phenomena for the methanation of CO2 and CO mixed syngas on a Ni/Al2O3 catalyst

Original
Kinetic study and deactivation phenomena for the methanation of CO2 and CO mixed syngas on a Ni/Al2O3 catalyst / Celoria, F., Salomone, F., Tauro, A., Gandiglio, M., Ferrero, D., Champon, I., Geffraye, G., Pirone, R., Bensaid, S.. - In: CHEMICAL ENGINEERING JOURNAL. - ISSN 1385-8947. - 512:(2025). [10.1016/j.cej.2025.162113]

Publisher:
Elsevier

Published
DOI:10.1016/j.cej.2025.162113

Chemical Engineering Journal 512 (2025) 162113

Contents lists available at ScienceDirect

Chemical Engineering Journal

journal homepage: www.elsevier.com/locate/cej

Kinetic study and deactivation phenomena for the methanation of CO_2 and CO mixed syngas on a Ni/Al_2O_3 catalyst☆

Fabrizio Celoria [a,1], Fabio Salomone [a,1,*], Alessio Tauro [a], Marta Gandiglio [b], Domenico Ferrero [b], Isabelle Champon [c], Geneviève Geffraye [c], Raffaele Pirone [a], Samir Bensaid [a]

[a] Catalytic Reaction Engineering for Sustainable Technologies (CREST) Group, Department of Applied Science and Technology (DISAT), Politecnico di Torino, Corso Duca degli Abruzzi 24, 10129 Torino, Italy
[b] Department of Energy (DENERG), Politecnico di Torino, Corso Duca degli Abruzzi 24, 10129 Torino, Italy
[c] Université Grenoble Alpes, CEA LITEN, DTCH, Laboratoire Réacteurs et Procédés (LRP), F-38000 Grenoble, France

A R T I C L E I N F O

Keywords:
Methanation
Nickel-alumina catalyst
Intrinsic kinetics
Deactivation
Power-to-gas

A B S T R A C T

This study presents a detailed kinetic and deactivation analysis of a 24 wt% Ni/Al_2O_3 catalyst for the hydrogenation of CO_2 and CO to CH_4, focusing the attention on the CO_2 and CO co-methanation. More than 300 reaction conditions were tested on a fixed-bed reactor obtaining 907 observations. Among them, 852 measurements were used to derive the kinetic parameters in an isothermal reactor model. Power-law models accurately describe CO_2 or CO methanation, but fail to predict co-methanation due to preferential adsorption of CO. On the contrary, a three-reactions Langmuir-Hinshelwood-Hougen-Watson model (model M4) successfully described it together with the different hydrogenation pathways. Experimental and literature insights suggest that CO_2 adsorption occurs via either dissociative or H-assisted associative mechanism, and then, the high H* coverage favors its conversion into CH_4 via the so-called dissociative formyl (CHO*) route. On the contrary, the exergonic CO adsorption increases the CO* coverage promoting the dissociative carbon (C*) route. In addition, C* species are responsible for the higher deactivation rates in CO methanation due to the formation of nickel carbides and coking. Long-term stability tests revealed several deactivation phenomena. CO_2 methanation induced mild sintering, while CO methanation led to a significant decrease in stability. Notably, co-methanation improved stability at low temperature by suppressing nickel carbide formation. Contaminants like O_2 and C_2H_4 decreased the stability due to re-oxidation and coking, respectively, while poisons like H_2S deactivated the catalyst irreversibly. Power-law deactivation models were developed to predict the activity loss, supporting the potential scale-up of CO_2 and CO methanation processes.

1. Introduction

Fighting climate change has become one of the most important challenges in recent decades. Many Countries have made major commitments to reduce greenhouse gas emissions, signing the Kyoto Protocol first and the Paris Agreement later. In addition, the 2030 Agenda, adopted by the United Nations places sustainable development as a global plan of action. A large part of the emissions come from the use of non-renewable energy sources, which are also the largest source of energy. According to data provided by the IEA, in 2022, the World's largest energy sources were oil (30.2 % of total energy supply), coal (27.6 %) and natural gas (23.1 %) [1]. Investment in fossil fuels is set to increase due to global overcrowding, as are greenhouse gas emissions, particularly carbon dioxide (CO_2). Energy-related CO_2 emissions are steadily increasing with a maximum reached in 2023 of 37.4 Gt, an increase of 8.6 % over the previous year [1]. Renewable energy sources, such as wind, solar and hydropower, are sustainable alternatives to fossil fuels and significant investments are currently being directed towards this sector. A crucial drawback of some of these technologies is the intermittent production of energy. As a result, energy storage is decisive to ensure stable supply, which can be achieved through batteries, that is

---

☆ This article is part of a special issue entitled: 'ISCRE 28' published in Chemical Engineering Journal.

* Corresponding author.

E-mail address: fabio.salomone@polito.it (F. Salomone).

[1] These authors contributed equally to this work.

https://doi.org/10.1016/j.cej.2025.162113

Nomenclature

Acronyms and Abbreviations

BET	Brunauer-Emmett-Teller
BJH	Barrett-Joyner-Halenda
BSE	Back-scattered electron
DFT	Density functional theory
DRIFTS	Diffuse reflectance infrared Fourier transform spectroscopy
EDS	Energy dispersive spectroscopy
FE-SEM	Field emission scanning electron microscopy
FID	Flame ionization detector
GC	Gas chromatograph
H_2-TPR	Temperature-programmed reduction under H_2 flow
HAADF	High-angle annular dark field
IEA	International Energy Agency
LHHW	Langmuir-Hinshelwood-Hougen-Watson
NDIR	Non-dispersive infrared
PFR	Plug-flow reactor
PL	Power-law
PL-CO2	Power-law for CO_2 methanation
PL-COI	Power-law with CO* inhibition
PL-HI	Power-law with H* inhibition
PtG	Power-to-Gas
RDS	Rate determining step
RWGS	Reverse water gas shift
SE	Secondary electron
SSA	Specific surface area (m^2/g)
TCD	Thermal conductivity detector
TEM	Transmission electron microscopy
XRD	X-ray diffraction

Parameters

a	Catalyst activity (dimensionless)
$a_{i,j,k}^{exp}$	Experimental activity of the i-th species at the j-th time on stream for the k-th stability test (dimensionless)
$a_{i,j,k}^{mod}$	Modeled activity of the i-th species at the j-th time on stream for the k-th stability test (dimensionless)
$a_{m,Ni}$	Average area occupied by a Ni atom on a polycrystalline surface ($6.21 \cdot 10^{-20}$ m^2/Ni atom)
a_{Ni}	Lattice constant of nickel assuming a face-centered cubic crystal structure ($3.52 \cdot 10^{-10}$ m)
$\widehat{c}_{p,g}$	Mass specific heat capacity of the gas (J/kg/K)
$c_{p,m}$	Specific volumetric heat capacity of the catalytic bed ($J/m^3/K$)
$\widehat{c}_{p,s}$	Specific mass heat capacity of the catalyst (J/kg/K)
D_{Ni}	Dispersion of nickel (dimensionless)
d	Order of deactivation (dimensionless)
d_t	Tube diameter (m)
$d_{VA,Ni}$	Volume-area mean diameter of the Ni particles (m)
$E_{A,\alpha}$	Activation energy of the α-th reaction (J/mol)
$E_{d,\beta}$	Activation energy for the deactivation phenomena for the β-th deactivation rate (J/mol)
F_D	Objective function for the deactivation regression model (dimensionless)
F_K	Objective function for the intrinsic kinetics regression model (dimensionless)
$K_{eq,\alpha}$	Equilibrium constant of the α-th reaction ($bar^{\Delta\nu_\alpha}$)
K_i	Van't Hoff adsorption constant of the i-th adsorbed species ($bar^{-n_{i,\alpha}}$)
K_{i,T_0}	Pre-exponential factor of the i-th adsorbed species at T_0 ($bar^{-n_{i,\alpha}}$)
k_{d,β,T_0}	Pre-exponential deactivation factor of the β-th deactivation rate at T_0
k_α	Kinetic constant of the α-th reaction
k_{α,T_0}	Arrhenius' pre-exponential factor of the α-th reaction at T_0
M_i	Molecular mass of the i-th chemical species (kg/mol)
$\dot{n}_{i,k}^{in}$	Inlet molar flow rates of the i-th component for the k-th experiment (mol/s)
$\dot{n}_{i,k}^{out}$	Outlet molar flow rates of the i-th component for the k-th experiment (mol/s)
$n_{i,\alpha}$	Exponent of the partial pressure for the i-th component for the α-th reaction (dimensionless)
n_{Ni}	Number of atoms on each face of the nickel crystal (dimensionless)
N_A	Avogadro's constant ($6.022 \cdot 10^{-23} mol^{-1}$)
N_c	Total number of chemical species (dimensionless)
N_e	Total number of experiments (dimensionless)
N_s	Total number of stability tests (dimensionless)
$N_{s,Ni}$	Number of exposed nickel atoms on the surface (dimensionless)
N_t	Total number of measurements during a stability test (dimensionless)
$N_{t,Ni}$	Total number of nickel atoms (dimensionless)
N_r	Total number of reactions (dimensionless)
p_i	Partial pressure of the i-th chemical species (bar)
$q_{i,\beta}$	Exponent of the gas concentration of the i-th component for the β-th deactivation (dimensionless)
Q_i	Reaction quotient of the i-th reaction ($bar^{\Delta\nu_\alpha}$)
R	Ideal gas constant (8.314 J/mol/K)
$r_{i,k}$	Molar reaction rate of the i-th species for the k-th stability test (mol/kg/s)
r_α	Molar reaction rate of the key component for the α-th reaction (mol/kg/s)
t	Sampling time (s)
T	Temperature (K)
t_0	Initial time of the stability test (s)
T_0	Reference temperature (598 K)
$v_{m,Ni}$	Average volume occupied by a Ni atom ($1.1 \cdot 10^{-29}$ m^3/Ni atom)
v_z	Superficial gas velocity along the axial coordinate z (m/s)
w_i	Mass fraction of the i-th chemical species (dimensionless)
$y_{i,j}^{exp}$	experimental molar fraction of the i-th species for the j-th experiment (dimensionless)
$y_{i,j}^{mod}$	modeled molar fraction of the i-th species for the j-th experiment (dimensionless)
$\Delta_r\widetilde{G}_{298K}^0$	Molar Gibbs' free energy variation of the reaction at 25 °C and 1 bar (kJ/mol)
$\Delta H_{i,\alpha}$	Adsorption enthalpy of the i-th component for the α-th reaction (J/mol)
$\Delta_r\widetilde{H}_{298K}^0$	Molar enthalpy variation of the reaction at 25 °C and 1 bar (kJ/mol)
$\Delta_r\widetilde{H}_\alpha$	Molar enthalpy of reaction of the key component of the α-th reaction (J/mol)
$\Delta\nu_\alpha$	Variation of the total number of moles of the α-th reaction (dimensionless)
ε_b	Bed void fraction of the catalytic bed (dimensionless)
ε_p	Intraparticle void fraction (dimensionless)
ε_t	Total void fraction of the reactor (dimensionless)
$\nu_{i,\alpha}$	Stoichiometric coefficient of the i-th component for the α-th reaction (dimensionless)
ρ_i	Density of the i-th chemical species (kg/m^3)
ρ_g	Density of the gas (kg/m^3)
ρ_{Ni}	Density of Ni metal (8900 kg/m^3)
ρ_s	Apparent skeletal density of the catalyst in the diluted catalytic bed (kg/m^3)

one of the most expensive solutions [2], or through Power-to-Gas (PtG) technology [3,4]. The main advantage of PtG technology is the conversion of electric energy into a stable energy carrier (e.g., CH_4) that can be easily used and transported, potentially replacing fossil-based natural gas and thus reducing CO_2 emissions from non-renewable energy sources [2,3,5]. Methane can be produced by combining H_2, that can be produced via electrolysis or pyrolysis, with CO_2, that is generally obtained through carbon capture technologies [6].

The methanation process consists of three reactions: the CO_2 hydrogenation to CH_4, known as the Sabatier's reaction, the CO hydrogenation to CH_4 and the reverse water gas shift (RWGS) reaction, as reported in equations (1) to (3) [7].

$$CO_{2(g)} + 4H_{2(g)} \leftrightarrow CH_{4(g)} + 2H_2O_{(g)} \; \Delta_r\widetilde{H}^0_{298K} = -165\frac{kJ}{mol} \; \Delta_r\widetilde{G}^0_{298K} = -114\frac{kJ}{mol} \tag{1}$$

$$CO_{(g)} + 3H_{2(g)} \leftrightarrow CH_{4(g)} + H_2O_{(g)} \; \Delta_r\widetilde{H}^0_{298K} = -206\frac{kJ}{mol} \; \Delta_r\widetilde{G}^0_{298K} = -142\frac{kJ}{mol} \tag{2}$$

$$CO_{2(g)} + H_{2(g)} \leftrightarrow CO_{(g)} + H_2O_{(g)} \; \Delta_r\widetilde{H}^0_{298K} = 41\frac{kJ}{mol} \; \Delta_r\widetilde{G}^0_{298K} = 29\frac{kJ}{mol} \tag{3}$$

Both methanation reactions (see equations (1) and (2)) are exothermic and number-of-moles consuming and, therefore, they are favored at low temperatures and high pressure. Although thermodynamically favored, the reduction of CO_2 and CO to methane has significant kinetic limitations because of the high stability of the molecules. Hence, the process is carried out on a heterogeneous catalyst to achieve high conversion and CH_4 yield [8].

Supported Ni catalysts are the most widely used industrial catalysts as they are highly efficient and significantly less expensive than noble metals. In particular, Ni/Al_2O_3 has been widely studied due to its good activity [9]. On the one hand, it has been found that Al_2O_3 could weaken the interaction between Ni particles and thus inhibit sintering. On the other hand, Al_2O_3 could promote solid C adsorption because of their affinity [10]. Hence, to improve performance, different oxides such as TiO_2, ZrO_2, CeO_2 and zeolites, are commonly employed as Ni supports, or are partially added to Al_2O_3 [4,11]. The optimal support is crucial for catalytic performance as it stabilizes the active site under reaction conditions and promotes adsorption of key reactants. In addition to nickel, other transition metals of the group VIII are also used for the methanation reaction [12,13]. Ru has been shown to be the most active element, however, its high cost and lower selectivity compared to other catalysts limit its use [14]. Less reactive than Ru and Ni, are Pd, Pt, Mo and Rh, which have higher selectivity toward CH_4. Other elements such as Fe, Co or Mo can lead to the formation of unsought by-products (e.g., methanol or hydrocarbons) [9,13].

Despite the fruitful studies conducted on methanation catalysts, there are still debates regarding the reaction pathways, the reaction mechanism and the rate-determining steps on Ni-based catalysts [15]. The pioneering research work by Weatherbee and Bartholomew [16] in 1982 was carried out on CO_2 methanation over Ni/SiO_2 catalyst. They proposed a dissociative carbon mechanism for CH_4 formation. It consists of a dissociative adsorption of CO_2 into adsorbed carbonyl (CO*) and atomic oxygen (O*) followed by the dissociation of CO* into carbon (C*) and O*. The C* species are subsequently hydrogenated to carbyne (CH*), carbene (CH_2*), methyl radical (CH_3*) and, lastly, to methane (CH_4*). Their kinetic study led to carbonyl dissociation being considered the most consistent RDS. A few years later, in 1989, Xu and Froment [17] thoroughly and extensively explored methane steam reforming, RWGS reaction and methanation considering a three-reactions system and proposing a dissociative formyl mechanism on 15 wt% $Ni/MgAl_2O_3$ catalyst. The hypothesized reaction mechanism describes the RWGS reaction via dissociative adsorption of CO_2 into CO* and O* and the hydrogenation of all carbonyl species into formyl groups (CHO*) prior to their hydrogenation to hydroxycarbene (CH_2O*) and decomposition into methylene groups (CH_2*) and O*. Notwithstanding their comprehensive work, the suggested model generally does not provide a good prediction for CO or CO_2 methanation on Ni-based catalysts.

Twenty years later, researchers have made significant progress in understanding the reaction mechanisms of CO methanation first, and of CO_2 methanation later over Ni-based catalysts. In 2010, Kopyscinski et al. [18] have extensively examined the CO hydrogenation mechanism over 50 wt% Ni/Al_2O_3 considering both dissociative routes. Their statistical approach indicated three equally possible RDS for the reaction mechanism: the C* hydrogenation to CH*, the hydrogenation of CH* to CH_2*, and the H-assisted dissociation of carbon-hydroxyl (COH*) into CH* and OH*. The dissociative carbon mechanism seems to be the most reliable, corroborating the work of Underwood and Bennett (1984) [19] on transient CO hydrogenation over nickel, although further investigations are required to clearly understand the reaction pathway. On the contrary, in 2016, Koschany et al. [20] have successfully described the CO_2 methanation over co-precipitated $NiAl(O)_x$ by means of the dissociative adsorption of CO_2 and the dissociative formyl (CHO*) mechanism, excluding the formation of intermediate C* species. This mechanism has been used by Marocco at al. (2018) [21] and Morosanu et al. (2020) [22] to investigate the catalytic activity of $NiAl(O)_x$ hydrotalcite and 20 wt% Ni/Al_2O_3 for CO_2 methanation, respectively. In the meantime, in 2019, Champon et al. [7] have developed a three-expressions kinetic model for both CO and CO_2 methanation and RWGS reaction over 15 wt% Ni/Al_2O_3. Their kinetic study has been founded on the reaction schemes already proposed in the literature [16,17,23].

More recently, in 2021, Burger et al. [15] and Schmider et al. [24] have conducted two parallel studies on CO-CO_2 co-methanation over a co-precipitated 44 wt% $NiAl(O)_x$ and supported Ni-based catalysts, respectively. Burger at al. [15] have proved by means of steady-state D_2 isotope tests and statistical model discrimination that the hydroxycarbene (CH_2O*) decomposition is the kinetically limiting step in methanation over the $NiAl(O)_x$ catalyst. In contrast, Schmider et al. [24] have a different approach developing a thermodynamically consistent microkinetic model for the CO and CO_2 methanation over Ni(111) surface. They have clearly shown that the dissociative carbon mechanism occurs in CO methanation, while associative carboxyl (COOH*) or formate (CHO_2*) occurs in CO_2 methanation prior to its dissociation into CO* and OH* and the subsequent C-O bond cleavage to form C* and O*. Similar conclusions have been obtained by Mohan et al. [14] by performing a DFT-assisted microkinetic modeling of the CO_2 methanation reaction on the Ni(111) surface as schematized in Fig. 1.

In the meantime, Cárdenas-Arenas et al. [25] have carried out DRIFTS and isotopic measurements discovering that there are two different active sites where H_2 and CO_2 chemisorb and dissociate over Ni/CeO_2 catalysts, while over Ni/Al_2O_3 there are no specific active sites. In both cases, the associative formate route seems to be the most truthful mechanism for CO_2 methanation. This research work paved the way for the kinetic studies of Quindimil et al. [26] on 9.5 wt% Ni/Al_2O_3 catalysts and Onrubia-Calvo et al. [11] on 8.5 wt% Ni/CeO_2. On the one hand, Quindimil et al. [26] have proposed an associative formate CO_2 adsorption followed by its dissociation into CO* before its hydrogenation into CHO*, using a one-active site scheme. On the other hand, Onrubia-Calvo et al. [11] have demonstrated that CO_2 methanation occurs via complete associative formate mechanism on two active sites without forming intermediate carbonyl or carbide species. Table 1 summarizes the state-of-the-art on the kinetic models for Ni-based catalysts. It is worth noting that the most significant aspects are the equilibrium distance, the prediction of the CO* inhibition in CO methanation and OH* inhibition both in CO and CO_2 methanation [16,18,20,26].

Together, these studies consistently indicate that CO_2 methanation occurs via dissociative formyl (CHO*) mechanism over Ni-based catalysts, while its chemisorption mechanism remains under debate and could occur via dissociative carbonyl or associative formate

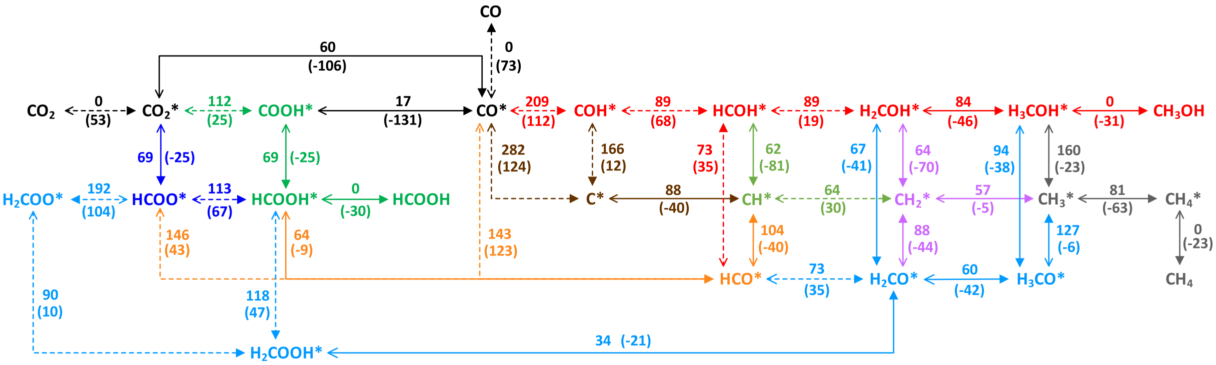

Fig. 1. Reaction pathways of the CO_2 hydrogenation on Ni (111) surface at 550 K and 10 bar resulting from the DFT-assisted microkinetic modeling presented by Mohan et al. [14]. Free energy barriers and reaction free energies (in brackets) are specified on the bidirectional arrows and refer to the direction indicated by the solid arrowhead. For the sake of clarity, endergonic reactions are denoted with dashed arrows.

Table 1
Most representative kinetic models present in the literature.

Type	Catalyst	T (°C)	P (bar)	Rate equations	Ref.
CO methanation and RWGS reaction	Ni/Al_2O_3	280–360	1–2	$r_{CH_4} = \frac{k_1 K_C p_{CO}^{0.5} p_{H_2}^{0.5}}{\left(1 + K_C p_{CO} + K_{OH} p_{H_2O} p_{H_2}^{-0.5}\right)^2}$ $r_{CO} = \frac{k_2\left(K_\alpha p_{CO} p_{H_2O} - p_{CO_2} p_{H_2} K_{eq}^{-1}\right)}{P_{H_2}^{0.5} \cdot \left(1 + K_C p_{CO} + K_{OH} p_{H_2O} p_{H_2}^{-0.5}\right)^2}$	[18]
CO methanation and RWGS reaction	Ni/Al_2O_3	315–430	2–6	$r_{CH_4} = \frac{k_1 p_{CO} p_{H_2}^{0.5}\left(1 - \frac{p_{CH_4} p_{H_2O}}{p_{CO} p_{H_2}^3 K_{eq}}\right)}{\left(1 + \sqrt{K_{H_2} p_{H_2}} + K_{CO_2} p_{CO_2} \sqrt{K_{H_2} p_{H_2}} + K_{OH} p_{H_2O} p_{H_2}^{-0.5} + K_{CO} p_{CO}\right)^2}$ $r_{CO} = \frac{k_2 p_{CO} p_{H_2}^{0.5}\left(1 - \frac{p_{CO} p_{H_2O}}{p_{CO_2} p_{H_2} K_{eq}}\right)}{\left(1 + \sqrt{K_{H_2} p_{H_2}} + K_{CO_2} p_{CO_2} \sqrt{K_{H_2} p_{H_2}} + K_{OH} p_{H_2O} p_{H_2}^{-0.5} + K_{CO} p_{CO}\right)^2}$	[26]
CO_2 methanation	NiAl(O)$_x$	180–340	1–15	$r_{CH_4} = \frac{k p_{H_2}^{0.5} p_{CO_2}^{0.5}\left(1 - \frac{p_{CH_4} p_{H_2O}^2}{p_{CO_2} p_{H_2}^4 K_{eq}}\right)}{\left(1 + K_{OH} p_{H_2O} p_{H_2}^{-0.5} + K_{H_2} p_{H_2}^{0.5} + K_{mix} p_{CO_2}^{0.5}\right)^2}$	[20,21]
CO_2 methanation	Ni/CeO_2	250–500	1.4–6	$r_{CH_4} = \frac{k p_{CO_2} p_{H_2}^{0.5}\left(1 - \frac{p_{CH_4} p_{H_2O}^2}{p_{CO_2} p_{H_2}^4 K_{eq}}\right)}{\left(1 + K_{H_2} p_{H_2}^{0.5}\right) \cdot \left(1 + K_{CO_2} p_{CO_2} + K_{H_2O} p_{H_2O} + K_{OH} p_{H_2O} p_{H_2}^{-0.5}\right)}$	[11]

intermediates. On the contrary, CO methanation seems to occur via dissociative carbon pathway over supported Ni catalyst and via dissociative formyl route over Ni hydrotalcites or co-precipitated catalysts. These two different reaction mechanisms may help explain the higher stability of co-precipitated NiAl(O)$_x$ in comparison to supported Ni/Al_2O_3 catalysts.

To develop active and stable catalysts, a thorough understanding of the mechanisms that lead to deactivation is crucial. In the literature, the deactivation of Ni-based catalysts is primarily linked to sintering, poisoning and carbon deposition [10,27].

Thermal sintering is ascribed to transport phenomena of metal atoms, particles or larger aggregates. Depending on the reaction temperature, the sintering process follows two growth mechanisms: particles move colliding and coalescing at low temperature, whilst atom migration prevails at high temperatures causing a reduction of the exposed Ni surface area [27,28]. More in detail, Champon et al. [29] have studied the sintering of Ni supported on γ-Al_2O_3, investigating the activity of fresh and spent catalysts under hydrothermal conditions with long-time tests. By increasing time, both CO_2 conversion and CH_4 yield decreased over time, and the loss of activity was ascribed to the decrease in metal surface area [27,29]. Moreover, Ewald et al. [30] have compared the activity loss of co-precipitated and impregnated Ni-based catalysts at different temperatures by feeding a stoichiometric H_2/CO_2 gas mixture. They have emphasized that co-precipitated catalysts are deactivated by a growth of Ni particles accompanied by a decrease of the CO_2 adsorption capacity and structural changes, whilst supported ones are mainly affected by sintering of metal particles and loss of specific surface area [30]. Besides temperature, the composition has a significant effect on the catalytic stability, which increases as the Ni content diminishes. Hence, thermal sintering is mitigated by reducing the specific activity of the catalytic material and consequently the probability of having hot spots in the reactor. Abelló et al. [31] and Garbarino et al. [32] have pointed out that excessive Ni content accelerates sintering and can lead to increased CO production.

Nickel is remarkably susceptible to poisoning by streams that contain S, P, Pb, NH_3 and C_2H_2. Among these, sulfur compounds are the most problematic because they are commonly present in the feed. Specifically, H_2S is generally produced during anaerobic digestion and pyrolysis of biomasses. In the literature, has been reported that the presence of very low concentrations of H_2S or SO_2 (around 5 ppm) are detrimental to the Ni-based catalyst provoking a complete deactivation due to the formation of stable NiS [27,33].

Lastly, solid carbon deposition can be avoided by working with higher H/C or O/C ratios so as to fall as far as possible from the carbon deposition zone [3]. It is worth noting that carbon deposition is a more significant issue in CO methanation under stoichiometric conditions, while it is less problematic in CO_2 methanation [27].

This work presents a kinetic modeling of CO_2 and CO methanation, focusing on the co-methanation process and on the effects of contaminants (C_2H_4 and O_2) and poisons (H_2S). As far as the objectives are concerned, a three-reaction LHHW kinetic model has been developed to describe all the reaction pathways (CO_2 methanation, CO methanation and CO-CO_2 co-methanation) on a 24 wt% Ni/Al_2O_3 catalyst. The experimental campaign was performed to represent all operating conditions (more than 900 observations) for obtaining the kinetic model. The effect of temperature, composition of the reactant mixture and the presence of contaminants such as O_2 and C_2H_4 and poisons such as H_2S will be shown. Deactivation constants and an operative map will be reported to identify the most favorable conditions for scaling-up the methanation process.

2. Methodology

2.1. Experimental campaign

2.1.1. Laboratory-scale test bench used for kinetic and deactivation tests

The experimental apparatus used for the kinetic and deactivation tests is shown in Supplementary Fig. S1. The gases, coming from cylinders (Gas / purity: H_2 4.5, CO_2 4.0, CO 3.7, N_2 6.0, CH_4 3.5), were accurately blended using mass-flow controllers electrically connected to the control system. Depending on the position of three pneumatic valves, the reactants could be directly fed to the reactor or bypass it to analyze their composition. The reactor was composed of a stainless-steel tube (o.d. 12 mm, i.d. 10 mm, length 350 mm) and an inner coaxial quartz tube (o.d. 6 mm, i.d. 4 mm). The catalytic bed was placed within the quartz tube and between two layers of SiC pellets. The whole reactor was heated by an electric oven and two thermocouples were used to measure and control the temperature. The first one was placed within the quartz tube at the end of the catalytic bed to measure the maximum temperature of reaction, while the second was placed in the middle of the oven in contact with the outer surface of the stainless-steel tube at the same height of the catalytic bed because the oven has an isothermal profile length around its center.

After the reactor, the water vapor was condensed before the gas flowrate passed through the back-pressure controller. A three-way valve allowed us to measure the composition of the gas mixture by means of an Agilent Technologies 7980B GC System equipped with two columns (HP-PLOT/Q and Molesieve 5A), a thermal conductivity detector (TCD) and a flame ionization detector (FID) and an in-line Emerson X-Stream Gas Analyzer equipped with two non-dispersive infrared (NDIR) sensors and a TCD to monitor continuously CO, CO_2, and H_2 concentrations, respectively. A silica trap was placed between the GC and the gas analyzer to completely dehydrate the gas mixture. Thanks to the GC, we were able to measure also byproducts of the reaction, especially hydrocarbons with a chain length from C_2 to C_7.

2.1.2. Catalyst and pre-treatment procedure

The experiments were performed using 75 mg of 24 wt% Ni/Al_2O_3 catalyst diluted with 375 mg of SiC, keeping a ratio of 1/5 between the catalyst and the inert. The measured height of the catalytic bed was approximately 23 mm with a particle density of 1.6 g/cm^3. The catalytic pellets as well as the SiC pellets had a narrow particle size distribution centered at 266 μm.

The catalyst required an activation procedure to reduce NiO into metallic nickel and stabilize it. Pure hydrogen (6 NL/h) was fed to the reactor at 7 bar and 315 °C (heating rate: 5 °C/min) for 24 h. As a last step, the sample was cooled down in N_2 before starting the catalytic tests.

2.1.3. Experimental methodology of the kinetic tests

Prior to performing kinetic experiments, the catalyst underwent a degreening test to stabilize its performance at 400 °C (heating rate: 4 °C/min) and 5 bar for 18 h using 30 NL/h of gas with the following composition $H_2/CO_2/N_2$ equal to 4/1/10. Subsequently, kinetic tests were carried out subdividing them into three main groups depending on the key reactant (CO_2, CO or a mixture of both CO_2 and CO). The compositions of the different inlet gas mixtures and their flow rates are summarized in Supplementary Tables S1, S2 and S3. For CO_2 methanation group, the volumetric flow rate was varied between 30 and 90 NL/h, while the H_2/CO_2 ratio was varied from 2 to 10, for CO methanation group, instead, the volumetric flow rate was between 60 and 90 NL/h and H_2/CO ratio was between 4 and 10. For CO_2 and CO co-methanation tests, the compositions of CO_2 (1.1 vol% – 6.7 vol%), CO (1.1 vol% – 6.7 vol%), H_2 (26.7 vol% – 53.3 vol%), CH_4 (3.3 vol% – 10.0 vol%) were varied, keeping the flow rate at 90 NL/h. All these conditions were performed at two pressures (5 bar and 15 bar) and 6 temperatures (250 °C, 280 °C, 310 °C, 340 °C, 370 °C and 400 °C), resulting in a total of 360 different reaction conditions. This wide range was used to ensure a statistical representation of all conditions compared to the large number of unknown kinetic parameters, considering the presence of experimentally unstable points, equilibrium conditions and outliers. The reaction conditions were selected to avoid the carbon deposition zone, as depicted in Fig. 2.

2.1.4. Experimental methodology of the stability tests

Different long-term tests were performed to assess the stability of catalytic performance under different reaction conditions. The operative conditions of these tests are shown in Supporting Table S4. The gas compositions and the temperature were the main investigated parameters. However, by-products (ethylene) and contaminants (oxygen) were also fed to the reactor to monitor their effects. For understanding the extent and the cause of the deactivation, two activity tests were also performed before and after the stability test by feeding 60 NL/h ($CO_2/H_2/N_2$ equal to 1/4/25) at 5 bar varying the temperature from 250 °C to 400 °C. Lastly, in Section 3 of the Supporting Information File, the equations used for evaluating the catalyst performance are reported.

2.1.5. H_2S poisoning

To determine the total number of catalytic active sites, an H_2S adsorption test was conducted on the pre-reduced catalyst. The adsorption test was carried out in a dedicated test bench, called Waste2Watts [34,35], equipped with a fixed bed reactor (i.d. 22 mm) at ambient temperature and pressure by feeding 15 NL/h of gas (200

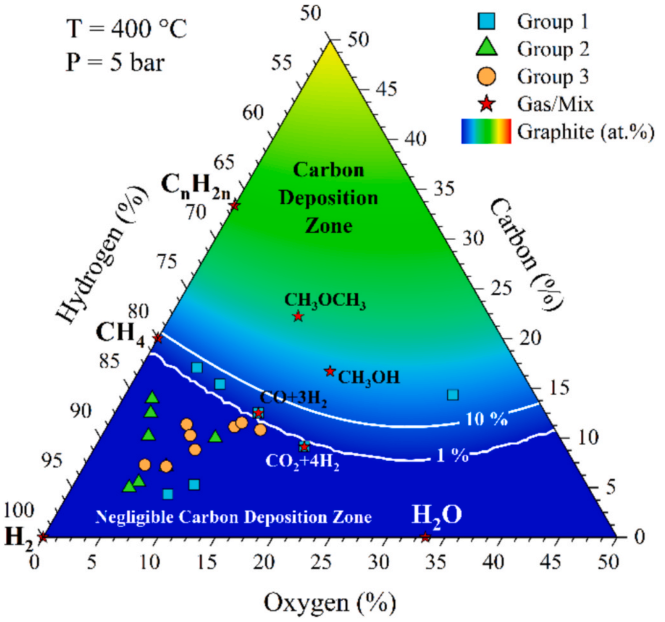

Fig. 2. C-H-O ternary diagram at 400 °C and 5 bar. The experimental conditions of the three groups of data are indicated on the diagram together with some significant gas species or mixtures.

ppm_{vol} H_2S/CH_4). The reactor was loaded with 0.45 g of pre-reduced Ni/Al_2O_3 catalyst diluted with quartz beads to have a bed height of 0.044 m. The gas composition was measured by using a MECCOS sensor H_2S detection from Siegrist GmbH. After poisoning, the residual activity of the poisoned catalyst was verified by feeding 60 NL/h ($CO_2/H_2/N_2$ equal to 1/4/25) at 5 bar ranging the temperature from 250 °C to 400 °C.

2.1.6. *Characterization of the catalyst*

N_2 physisorption, XRD, SEM, TEM and H_2-TPR measurements were employed to analyze the fresh catalyst and the effect of the activation procedure; moreover, XRD and SEM measurements were carried out on some specific samples to corroborate the proposed causes of deactivation.

More in detail, N_2 physisorptions were performed at −196 °C on the fresh and reduced catalyst employing a Micromeritics Tristar II ASAP 3020 analyzer. The samples were previously outgassed at 200 °C for 2 h under N_2 flow using a Micromeritics FlowPrep 060. The SSA was evaluated according to the BET equation and the pore size distribution was analyzed using the BJH algorithm on the desorption branch of the isotherm [36].

X-ray diffractograms were collected using a Malvern Panalytical Empyrean diffractometer equipped with a high-resolution Bragg-Brentano optical module. Data were recorded scanning the 2θ angle range 25° – 80° with a step size of 0.026° 2θ and a dwell time of 1.02 s per step, operating at 40 kV and 40 mA and using Ni β-filtered Cu-Kα radiation with a wavelength (λ) of 1.5406×10^{-10} m.

The H_2-TPR measurement was performed on the fresh catalyst using an AMI-300Lite instrument equipped with a TCD. The sample (20 mg) was placed between two layers of quartz wool in a quartz tube reactor (o.d. 6 mm, i.d. 4 mm) and pre-treated at 300 °C (heating rate: +10 °C/min) for 30 min with He (20 NmL/min) and then, it was cooled down to 50 °C. After that, the H_2-TPR analysis was carried out flowing 5.0 %vol. H_2/Ar (20 NmL/min) and heating the sample from 50 °C to 700 °C (heating rate: +10 °C/min, hold time: 30 min). The calibration was done with 10 gas pulses (0.524 mL/pulse of pure Ar) in a 5.0 %vol. H_2/Ar flow (20 mL/min) using a dedicated pipeline of the equipment.

Lastly, a Zeiss Merlin FE-SEM equipped with a Gemini II column and a FEI Tecnai F20ST TEM were employed to investigate in more detail the morphology of the catalyst. In addition, both instruments are equipped with an EDS detector to determine the elemental composition of specific portions of the samples.

2.2. *Kinetic modeling*

Along with the experimental campaign, the algorithm for simulating the reactor, fitting the kinetic parameters and optimizing the kinetic model was conceptualized as schematized in Fig. 3. A model of the experimental reactor was created in MATLAB environment to evaluate the performance of the reactor using a well-defined kinetic model of the reactions and assuming specific kinetic parameters. The modeled results were used along with the experimental ones to evaluate the objective function (i.e. residuals). At this stage, it was minimized by varying the kinetic parameters. Once the optimized kinetic parameters were obtained for a given kinetic model, the latter was modified, and new kinetic parameters were identified. Different kinetic models were compared to statistically identify the best one that represents the experimental data.

As far as the modeling of the reactor, an isothermal model was developed to fit both intrinsic and deactivation kinetic parameters. The experimental reactor was modeled as a pseudo-homogeneous, isobaric, one-dimensional plug-flow reactor (PFR) with negligible axial dispersion.

2.2.1. *Mass balance*

The continuity mass balance equation for a generic i-th chemical species along the axial coordinate of the reactor is described by equation (4) [37]. In the equation, the total void fraction of the reactor was evaluated using equation (5).

$$\varepsilon_t \cdot \frac{\partial \rho_i}{\partial t} + \frac{v_z}{\varepsilon_b} \cdot \frac{d\rho_i}{dz} = (1-\varepsilon_t)\cdot \rho_s \cdot a \cdot \sum_{\alpha=1}^{N_r} \left(M_i \cdot \nu_{i,\alpha} \cdot r_\alpha\right) \tag{4}$$

$$\varepsilon_t = \varepsilon_b + \varepsilon_p \cdot (1-\varepsilon_b) \tag{5}$$

For the sake of clarity, the intrinsic kinetic of the catalyst was obtained assuming the reactor in stationary conditions without catalyst deactivation ($a = 1$). While the regression of the deactivation parameters was performed by considering all the time-dependent terms of the balance equations.

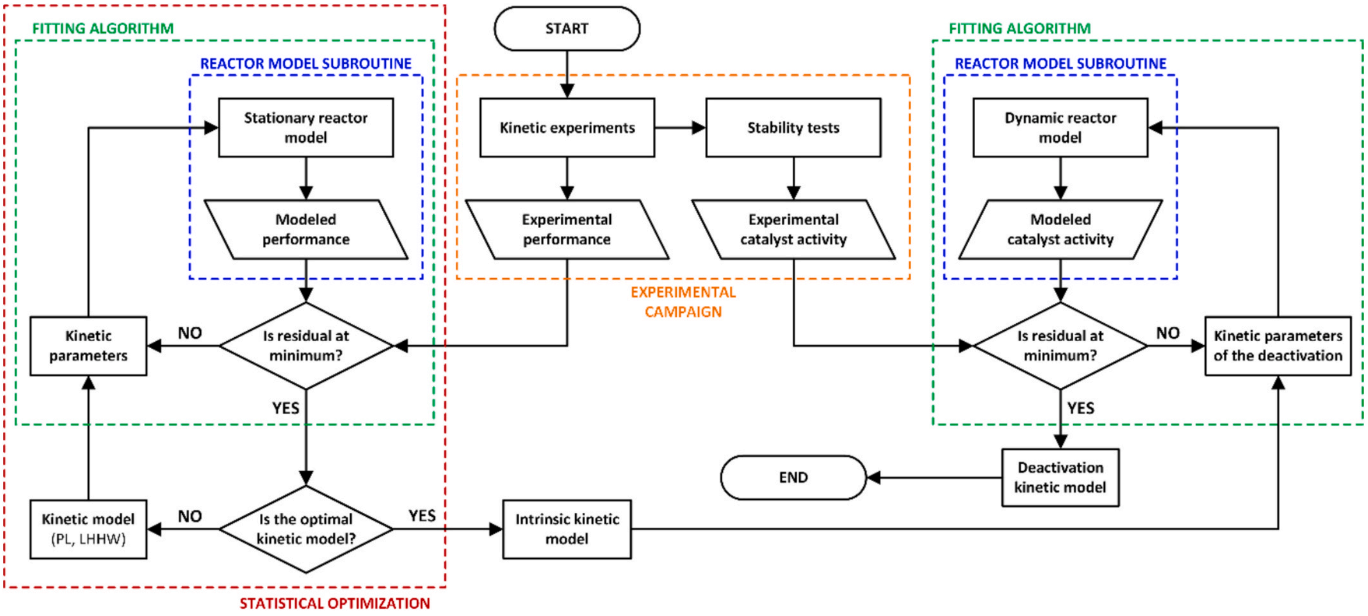

Fig. 3. Conceptual flowchart of the kinetic model fitting and optimization algorithms.

2.2.2. Thermodynamic and transport properties

In this work, the gas mixture was treated as ideal. Gas phase thermochemistry data were estimated according to the Shomate equation [38], while the reaction thermodynamic properties were evaluated according to the Hess' law. As far as the properties of the gas mixture, the Wassiljewa model was used to estimate the thermal conductivity of the gas mixture [41,42], while its dynamic viscosity was obtained using the Reichenberg model [39,40]. Binary diffusion coefficients were determined according to the Chapman-Enskog theory and the diffusivity of a species in the gas mixture was approximated using the Wilke model [37,40]. The intraparticle effective diffusivity was estimated according to the Bosanquet correlation considering both molecular and Knudsen diffusion coefficients [37]. All those correlations are exhaustively described in Section 4 of the Supporting Information File.

Both external and internal mass and heat transport criteria were verified before finding the intrinsic kinetic parameters and ensured that the experimental data were not affected by transport limitations. These criteria are described in Section 5 of the Supporting Information File. Moreover, in Supplementary Table S9, the characteristics of the reactor and of the catalyst are summarized.

2.2.3. Power-law kinetic models

Power-law (PL) kinetic expressions were the first to be considered to describe the methanation process. Firstly, equation (6) describes the CO_2 hydrogenation to methane (PL-CO2). Secondly, equation (7) describes the CO hydrogenation to methane considering the inhibiting effect of CO* species during CO methanation (PL-COI). Thirdly, equation (8) describes the RWGS reaction and it was formulated to consider the inhibiting effect of adsorbed H* species on the catalytic active sites (PL-HI).

$$r_1 = k_1 \cdot p_{CO_2}^{n_{CO_2,1}} \cdot p_{H_2}^{n_{H_2,1}} \cdot \left(1 - \frac{Q_1}{K_{eq,1}}\right) \; \textit{PL for } CO_2 \textit{ methanation } (PL - CO2) \tag{6}$$

$$r_2 = \frac{k_2 \cdot p_{H_2}^{n_{H_2,2}}}{1 + K_{CO,2} \cdot p_{CO}^{n_{CO,2}}} \left(1 - \frac{Q_2}{K_{eq,2}}\right) \; \textit{PL with } CO^* \textit{ inhibition } (PL - COI) \tag{7}$$

$$r_3 = \frac{k_3 \cdot p_{CO_2}^{n_{CO_2,3}}}{1 + K_{H_2,3} \cdot p_{H_2}^{n_{H_2,3}}} \cdot \left(1 - \frac{Q_3}{K_{eq,3}}\right) \; \textit{PL with } H^* \textit{ inhibition } (PL - HI) \tag{8}$$

The reaction quotients of each reaction are specified in equation (9) for the CO_2 methanation, in equation (10) for the CO methanation and in equation (11) for the RWGS reaction.

$$Q_1 = \frac{p_{CH_4} \cdot p_{H_2O}^2}{p_{CO_2} \cdot p_{H_2}^4} \tag{9}$$

$$Q_2 = \frac{p_{CH_4} \cdot p_{H_2O}}{p_{CO} \cdot p_{H_2}^3} \tag{10}$$

$$Q_3 = \frac{p_{CO} \cdot p_{H_2O}}{p_{CO_2} \cdot p_{H_2}} \tag{11}$$

In addition, the Arrhenius-type kinetic constants and the van't Hoff-type adsorption constants were evaluated according to equations (12) and (13), respectively.

$$k_\alpha = k_{\alpha,T_0} \cdot \exp\left[-\frac{E_{A,\alpha}}{R}\left(\frac{1}{T} - \frac{1}{T_0}\right)\right] \tag{12}$$

$$K_{i,\alpha} = K_{i,T_0,\alpha} \cdot \exp\left[-\frac{\Delta H_{i,\alpha}}{R}\left(\frac{1}{T} - \frac{1}{T_0}\right)\right] \tag{13}$$

2.2.4. LHHW kinetic models

Five different LHHW kinetic models were obtained by considering the reaction steps listed in Table 2. Models M1 and M2 were derived according to the literature [16,20,26]; while the following assumptions were made for models M3, M4 and M5: energy uniformity of active sites, monomolecular adsorbed layer, negligible interactions between

Table 2
Reaction steps considered for the derivation of the five LHHW models (M1–M5).

	Reactions	**M1** (Koschany et al. [20])	**M2** (Quindimil et al. [26])	**M3** (Schmider et al. [24])	**M4**	**M5**
(1)	$H_2(g) + * \rightleftarrows H_2^*$	Quasi-equilibrium	Low coverage	Reversible	Reversible	Reversible
(2)	$H_2^* + * \rightleftarrows 2H^*$	Quasi-equilibrium	Quasi-equilibrium	Reversible	Reversible	Reversible
(3)	$CO_2(g) + * \rightleftarrows CO_2^*$	–	–	Reversible	Reversible	Reversible
(4)	$CO_2(g) + OH^* \rightleftarrows HCO_3^*$	–	Quasi-equilibrium	–	–	–
(5)	$CO(g) + * \rightleftarrows CO^*$	–	–	–	–	Reversible
(6)	$CO_2(g) + 2* \rightleftarrows CO^* + O^*$	Quasi-equilibrium	–	–	Reversible	–
(7)	$CO_2^* + H^* \rightleftarrows COOH^* + *$	–	–	Reversible	Reversible	–
(8)	$CO_2^* + H^* \rightleftarrows CHO^* + O^*$	–	–	–	–	**RDS**
(9)	$CO_2^* + * \rightleftarrows CO^* + O^*$	–	–	–	–	**RDS**
(10)	$COOH^* + * \rightleftarrows CO^* + OH^*$	–	–	**RDS**	**RDS**	–
(11)	$HCO_3^* + H^* \rightleftarrows HCOO^* + OH^*$	–	Quasi-equilibrium	–	–	–
(12)	$HCOO^* + * \rightleftarrows CO^* + OH^*$	–	**RDS**	–	–	–
(13)	$CO^* \rightleftarrows CO(g) + *$	–	Quasi-equilibrium	Reversible	Reversible	–
(14)	$CO^* + H^* \rightleftarrows C^* + OH^*$	–	–	**RDS**	**RDS**	–
(15)	$C^* + H^* \rightleftarrows CH^* + *$	–	–	Reversible	Reversible	–
(16)	$CO^* + H^* \rightleftarrows CHO^* + *$	**RDS**	**RDS**	–	**RDS**	**RDS**
(17)	$CHO^* + * \rightleftarrows CH^* + O^*$	Low coverage	Low coverage	–	Reversible	–
(18)	$CHO^* + H^* \rightleftarrows CH_2O^* + *$	–	–	–	–	Reversible
(19)	$CH^* + H^* \rightleftarrows CH_2^* + *$	Low coverage	Low coverage	Reversible	Reversible	–
(20)	$CH_2O^* + * \rightleftarrows CH_2^* + O^*$	–	–	–	–	Reversible
(21)	$CH_2^* + H^* \rightleftarrows CH_3^* + *$	Low coverage	Low coverage	Reversible	Reversible	Reversible
(22)	$CH_3^* + H^* \rightleftarrows CH_4^* + *$	Low coverage	Low coverage	Reversible	Reversible	Reversible
(23)	$CH_4^* \rightleftarrows CH_4(g) + *$	Low coverage	Low coverage	Reversible	Reversible	Reversible
(24)	$O^* + H^* \rightleftarrows OH^* + *$	Irreversible	Low coverage	–	Reversible	–
(25)	$OH^* + H^* \rightleftarrows H_2O^* + *$	Quasi-equilibrium	Quasi-equilibrium	Reversible	Reversible	–
(26)	$H_2O^* \rightleftarrows H_2O(g) + *$	Quasi-equilibrium	Low coverage	Reversible	Reversible	–
(27)	$H_2(g) + O^* \rightleftarrows H_2O(g) + *$	–	–	–	–	Reversible

adsorbed particles, reversibility and validity of the mass action law.

Firstly, model M1 describes the reaction rate for the CO_2 methanation, and it was formulated according to Koschany et al. [20]. Model M1 predicts the CO_2 adsorption and carbon–oxygen bond cleavage forming CO* and its hydrogenation into formyl species (CHO). This model is only suitable to describe CO_2 methanation without considering the formation of gaseous CO. To overcome this limitation, models with at least two reactions are required to successfully describe the hydrogenation of both CO_2 and CO. Therefore, two models were derived by considering two different reaction routes: the dissociative formyl mechanism (M2) [26] and the dissociative carbon mechanism (M3) [24]. On the one hand, both models predict an H-assisted formation of CO* from CO_2, proceeding via a formate (HCOO*) intermediate in model M2, and a carboxyl (COOH*) intermediate in model M3. On the other hand, in model M2, the hydrogenation of CO* occurs through the formation of a formyl species; while, in model M3, CO* dissociates forming C*. Lastly, two different three-reactions models were derived: model M4 incorporates both dissociative formyl and dissociative carbon mechanisms, while model M5 accounts for the formation of formyl (CHO*) species from both CO_2 and CO [14]. In addition, in both these models CO_2 adsorption occurs via an H-assisted pathway, but in model M4, the CO_2 dissociative pathway was also considered. The kinetic expressions are given in Table 3, while their derivations are reported in Section S6 of the Supporting Information File.

2.2.5. Kinetic model of the deactivation

The deactivation of a catalyst could be described with an activity coefficient that depends on many aspects: temperature, pressure, reactions and physic-chemical interactions. The variation of the activity of a catalyst could be described by using a deactivation kinetic expression as reported in equation (25).

$$\frac{da}{dt} = -k_{d,T_0}\cdot\exp\left[\frac{-E_d}{R}\cdot\left(\frac{1}{T}-\frac{1}{T_0}\right)\right]\cdot f(C)\cdot a^d \tag{25}$$

In this equation, $f(C)$ is a function of the concentrations of the species that mainly affect the deactivation. In this work, the initial activity of the catalyst was assumed to be unitary, and all the reactions were considered equally affected by deactivation without changing the relative reaction rates. The catalyst under investigation can be affected by different deactivating phenomena: sintering, coking, oxidation and pollution. These phenomena prevail under certain reaction conditions and should be described specifically for each case of study within the operating conditions used for the tests.

2.2.6. Objective functions of the fitting algorithms

The regression of the intrinsic kinetic parameters was performed by minimizing the objective function defined in equation (26), that is a non-linear function of the residuals between experimental and modeled results.

$$F_K = \sum_{j=1}^{N_e}\sum_{i=1}^{N_c}\left(y_{i,j}^{exp}-y_{i,j}^{mod}\right)^2 \tag{26}$$

Similarly, the regression of the deactivation kinetic parameters was

Table 3
Reaction rate expressions for the LHHW-based kinetic models M1–M5.

Model	Reaction	Reaction rate expression	Equation
M1	CO_2 methanation	$r_1 = \frac{k_1\cdot p_{CO_2}^{0.5}\cdot p_{H_2}^{0.5}\cdot\left(1-\frac{Q_1}{K_{eq,1}}\right)}{\left(1+K_{H_2}\cdot p_{H_2}^{0.5}+K_{mix}\cdot p_{CO_2}^{0.5}+K_{OH}\cdot p_{H_2O}\cdot p_{H_2}^{-0.5}\right)^2}$	(14)
M2	CO methanation	$r_2 = \frac{k_2\cdot p_{CO}\cdot p_{H_2}^{0.5}\cdot\left(1-\frac{Q_2}{K_{eq,2}}\right)}{\left[1+K_{H_2}^{0.5}\cdot p_{H_2}^{0.5}\cdot\left(1+K_{CO_2}\cdot p_{CO_2}\right)+K_{OH}\cdot p_{H_2O}\cdot p_{H_2}^{-0.5}+K_{CO}\cdot p_{CO}\right]^2}$	(15)
	RWGS	$r_3 = \frac{k_3\cdot p_{CO_2}\cdot p_{H_2}^{0.5}\cdot\left(1-\frac{Q_3}{K_{eq,3}}\right)}{\left[1+K_{H_2}^{0.5}\cdot p_{H_2}^{0.5}\cdot\left(1+K_{CO_2}\cdot p_{CO_2}\right)+K_{OH}\cdot p_{H_2O}\cdot p_{H_2}^{-0.5}+K_{CO}\cdot p_{CO}\right]^2}$	(16)
M3	CO methanation	$r_2 = \frac{k_2\cdot p_{CO}\cdot p_{H_2}^{0.5}\cdot\left(1-\frac{Q_2}{K_{eq,2}}\right)}{\left(1+K_{H_2}^{0.5}\cdot p_{H_2}^{0.5}+K_{CO}\cdot p_{CO}+K_C\cdot p_{CH_4}\cdot p_{H_2}^{-2}+K_{CH_4}\cdot p_{CH_4}\right)^2}$	(17)
	RWGS	$r_3 = \frac{k_3\cdot p_{CO_2}\cdot p_{H_2}^{0.5}\cdot\left(1-\frac{Q_3}{K_{eq,3}}\right)}{\left(1+K_{H_2}^{0.5}\cdot p_{H_2}^{0.5}+K_{CO}\cdot p_{CO}+K_C\cdot p_{CH_4}\cdot p_{H_2}^{-2}+K_{CH_4}\cdot p_{CH_4}\right)^2}$	(18)
M4	CO_2 methanation	$r_1 = \frac{k_1\cdot p_{CO_2}\cdot p_{H_2}^{1.5}\cdot p_{H_2O}^{-1}\cdot\left(1-\frac{Q_1}{K_{eq,1}}\right)}{\left(1+K_{H_2}^{0.5}\cdot p_{H_2}^{0.5}+K_{CO}\cdot p_{CO}+K_C\cdot p_{CH_4}\cdot p_{H_2}^{-2}+K_{CH_4}\cdot p_{CH_4}\right)^2}$	(19)
	CO methanation	$r_2 = \frac{k_2\cdot p_{CO}\cdot p_{H_2}^{0.5}\cdot\left(1-\frac{Q_2}{K_{eq,2}}\right)}{\left(1+K_{H_2}^{0.5}\cdot p_{H_2}^{0.5}+K_{CO}\cdot p_{CO}+K_C\cdot p_{CH_4}\cdot p_{H_2}^{-2}+K_{CH_4}\cdot p_{CH_4}\right)^2}$	(20)
	RWGS	$r_3 = \frac{k_3\cdot p_{CO_2}\cdot p_{H_2}^{0.5}\cdot\left(1-\frac{Q_3}{K_{eq,3}}\right)}{\left(1+K_{H_2}^{0.5}\cdot p_{H_2}^{0.5}+K_{CO}\cdot p_{CO}+K_C\cdot p_{CH_4}\cdot p_{H_2}^{-2}+K_{CH_4}\cdot p_{CH_4}\right)^2}$	(21)
M5	CO_2 methanation	$r_1 = \frac{k_1\cdot p_{CO_2}\cdot p_{H_2}^{0.5}\cdot\left(1-\frac{Q_1}{K_{eq,1}}\right)}{\left(1+K_{H_2}^{0.5}\cdot p_{H_2}^{0.5}+K_{CO}\cdot p_{CO}+K_{H_2O}\cdot p_{H_2O}\cdot p_{H_2}^{-1}+K_{CH_4}\cdot p_{CH_4}\right)^2}$	(22)
	CO methanation	$r_2 = \frac{k_2\cdot p_{CO}\cdot p_{H_2}^{0.5}\cdot\left(1-\frac{Q_2}{K_{eq,2}}\right)}{\left(1+K_{H_2}^{0.5}\cdot p_{H_2}^{0.5}+K_{CO}\cdot p_{CO}+K_{H_2O}\cdot p_{H_2O}\cdot p_{H_2}^{-1}+K_{CH_4}\cdot p_{CH_4}\right)^2}$	(23)
	RWGS	$r_3 = \frac{k_3\cdot p_{CO_2}\cdot\left(1-\frac{Q_3}{K_{eq,3}}\right)}{\left(1+K_{H_2}^{0.5}\cdot p_{H_2}^{0.5}+K_{CO}\cdot p_{CO}+K_{H_2O}\cdot p_{H_2O}\cdot p_{H_2}^{-1}+K_{CH_4}\cdot p_{CH_4}\right)^2}$	(24)

performed by defining the objective function as reported in equation (27) and minimizing it. The catalytic activity ($a_{i,k}$) was estimated according to equation (28).

$$F_D = \sum_{k=1}^{N_s}\sum_{j=1}^{N_t}\sum_{i=1}^{N_c}\left(a_{i,j,k}^{exp} - a_{i,j,k}^{mod}\right)^2 \cong \sum_{k=1}^{N_s}\sum_{j=1}^{N_t}\left(a_{CH_4,j,k}^{exp} - a_{CH_4,j,k}^{mod}\right)^2 \tag{27}$$

$$a_{i,k}(t) = \frac{r_{i,k}(t)}{r_{i,k}(t_0)} = \frac{\dot{n}_{i,k}^{out}(t) - \dot{n}_{i,k}^{in}(t)}{\dot{n}_{i,k}^{out}(t_0) - \dot{n}_{i,k}^{in}(t_0)} \tag{28}$$

The minimization was carried out using MATLAB with the Statistics and Machine Learning Toolbox^{TM}. The kinetic parameters were firstly estimated using a genetic algorithm and subsequently non-linear fitting routines were employed to minimize the solution in a narrow range. Among all measurements, outliers may distort the result of the regression; thus, those with a Cook's distance greater than $4/N_e$ were excluded [41].

3. Results and discussion

The central section of this work seeks to provide the experimental results of the catalytic tests performed on the 24 wt% Ni/Al_2O_3 catalyst, the parameters of the intrinsic kinetic models and those of the deactivation rate expressions. In addition, it presents the characterizations of some specific samples to corroborate the experimental and modeled results.

3.1. *Characterization of the catalyst*

This section reports the results of characterization techniques performed on the catalyst focusing on the fresh and reduced sample. The analysis of the samples at the end of the stability test with CO_2/H_2 reactant mixture (see Table S4, test S3), with CO/H_2 reactant mixture (see Table S4, test S5), and at the end of the H_2S poisoning test are reported in paragraph 3.3.

The main outcomes of the N_2 physisorption analyses conducted on the fresh and reduced Ni/Al_2O_3 catalyst are reported in Fig. S2. The fresh catalyst exhibited a SSA_{BET} of 87.2 $m^2 \cdot g^{-1}$, a total pore volume of 0.241 $cm^3 \cdot g^{-1}$. After the reduction procedure, the SSA_{BET} and the total pore volume decreased to 85.4 $m^2 \cdot g^{-1}$ and 0.202 $cm^3 \cdot g^{-1}$, respectively. In addition, as can be seen in Fig. S2 a), the amount of nitrogen adsorbed by the two samples is very similar. These results demonstrate that the activation treatment did not cause severe particle sintering. Fig. S2 b) shows the pore size distribution of both samples that exhibit a maximum around 12 nm.

The H_2-TPR analysis (Fig. S3) demonstrates that the reduction of the catalyst starts at 300 °C and that the maximum signal is centered at 540 °C. Based on the consumed amount of H_2, it is possible to quantify the amount of NiO in the catalyst, which is 26 wt% NiO, a value consistent with the nominal mass fraction (24 wt% of Ni). The activation protocol involves reducing the material to 315 °C to avoid sintering of the active phase particles. The reduction of the sample at mild conditions is facilitated by the high H_2 partial pressure (7 bar) and the long treatment time (24 h).

The morphology of the fresh catalyst was investigated through SEM microscopy (Fig. S4). The average size of NiO particles is 200 nm, with some of them reaching 15 nm. Fig. S5 shows the SEM analysis carried out on the reduced sample. It is worth observing that the remaining O is present in the support and almost absent in the Ni, meaning that the activation procedure reduced the NiO. The morphology and the particle size did not change significantly, confirming that the activation procedure reduced NiO without causing severe sintering of the active phase. The structure of the catalyst was further investigated by XRD analysis. Compared to the EDS results of the SEM analysis, it can be observed in Fig. S6 that NiO is still present in the reduced sample, as evidenced by the presence of the peaks located at 37.2°, 43.3° and 62.9°. However, these three peaks are significantly less intense than those of the fresh sample. The semi-quantitative analysis performed on XRD diffractograms revealed that the mass fraction of NiO in the fresh sample is 32 wt %, whilst in the reduced sample about half of the NiO was reduced after the activation procedure (14 wt% Ni, 13 wt% NiO).

Fig. 4 displays the results of TEM microscopy conducted on the reduced catalyst. It is worth noting that the identified interplanar distances are consistent with those of metallic Ni and γ-Al_2O_3. In addition, as reported in Fig. 4 and in Fig. S7, STEM-EDS maps highlight the distribution of Ni particles in the samples that are present in the form of both dispersed nanoparticles and aggregates of larger particles.

3.2. *Intrinsic kinetic study*

Firstly, this section outlines the observations from the catalytic tests and then summarizes the kinetic parameters of the PL and LHHW kinetic models presented in the Methodology.

3.2.1. *Experimental observations*

The experimental results have been subdivided based on the influence of the following parameters: residence time, partial pressures of H_2, CO_2, CO and CH_4. The different behaviors are shown in Fig. 5 where CH_4 yield as a function of temperature is shown for tests conducted at 5 bar, while in Section 8 of the Supporting Information File, a more detailed comparison is shown considering also the tests at 15 bar. Since CO_2 and CO methanation reactions reduce the total number of moles, by Le Chatelier principle, an increase in the pressure of the system shifts the equilibrium favoring CH_4 production. Besides it, those reactions are extremely exothermic, provoking a non-negligible increase of the temperature in the reactor at high conversions. Hence, conversions close to thermodynamic equilibrium were reached in tests at high pressure and low flow rates. These experimental points were excluded from the kinetic regression because they were not represented by the model assumptions.

As previously described, the test conditions were divided into three groups: CO_2 methanation, CO methanation and CO-CO_2 co-methanation. For all conditions of group I (see Table S1), the CH_4 selectivity was always higher than 95 % up to temperatures close to 400 °C, while the CO yield remained below 5 %. Concerning the tests of group II (see Table S2), the CO_2 yield did not exceed 1 %, obtaining a CH_4 selectivity close to 100 %. This means that the WGS reaction is not favored. A similar result was obtained by Mohan et al. [14], which have conducted a DFT analysis on a Ni (111) surface, investigating the CO_2 methanation reaction mechanism. They have determined that CO adsorbs on the surface forming the CO* carbonyl group and that the energy required to form the CO_2* complex is greater than the energy required for the hydrogenation of CO*.

Considering the variation of the residence time for the group I tests, if it increases both the CO_2 conversion and the CH_4 yield rise, approaching to the equilibrium with the lowest flow rate (30 NL/h) around 400 °C at 5 bar and above 350 °C at 15 bar (see Fig. S8). In addition, reducing the residence time, the CO selectivity increases, meaning that CO is most likely an intermediate species in the reaction mechanism. On the contrary, the variation of the residence time did not affect the CH_4 yield in CO methanation experiments (group II) as can be seen in Fig. S9. This phenomenon was ascribed to the high affinity between the catalyst surface and CO, which is promptly adsorbed on it.

The increase of the CO_2 partial pressure in group I experiments (see Fig. S10) caused a decrease of the CH_4 yield in under-stoichiometric conditions ($H_2/CO_2 < 4$) and an increase in over-stoichiometric conditions ($H_2/CO_2 > 4$). Despite the difference observed in CH_4 yield, the CH_4 formation rate remained almost unchanged as the partial pressure of CO_2 changed. This result agrees with the literature, which also reports a weak dependence on the CO_2 partial pressure [7].

Analogously, in group II, the reduction of the CO partial pressure causes an increased CH_4 yield (see Fig. S11). Similar CH_4 production

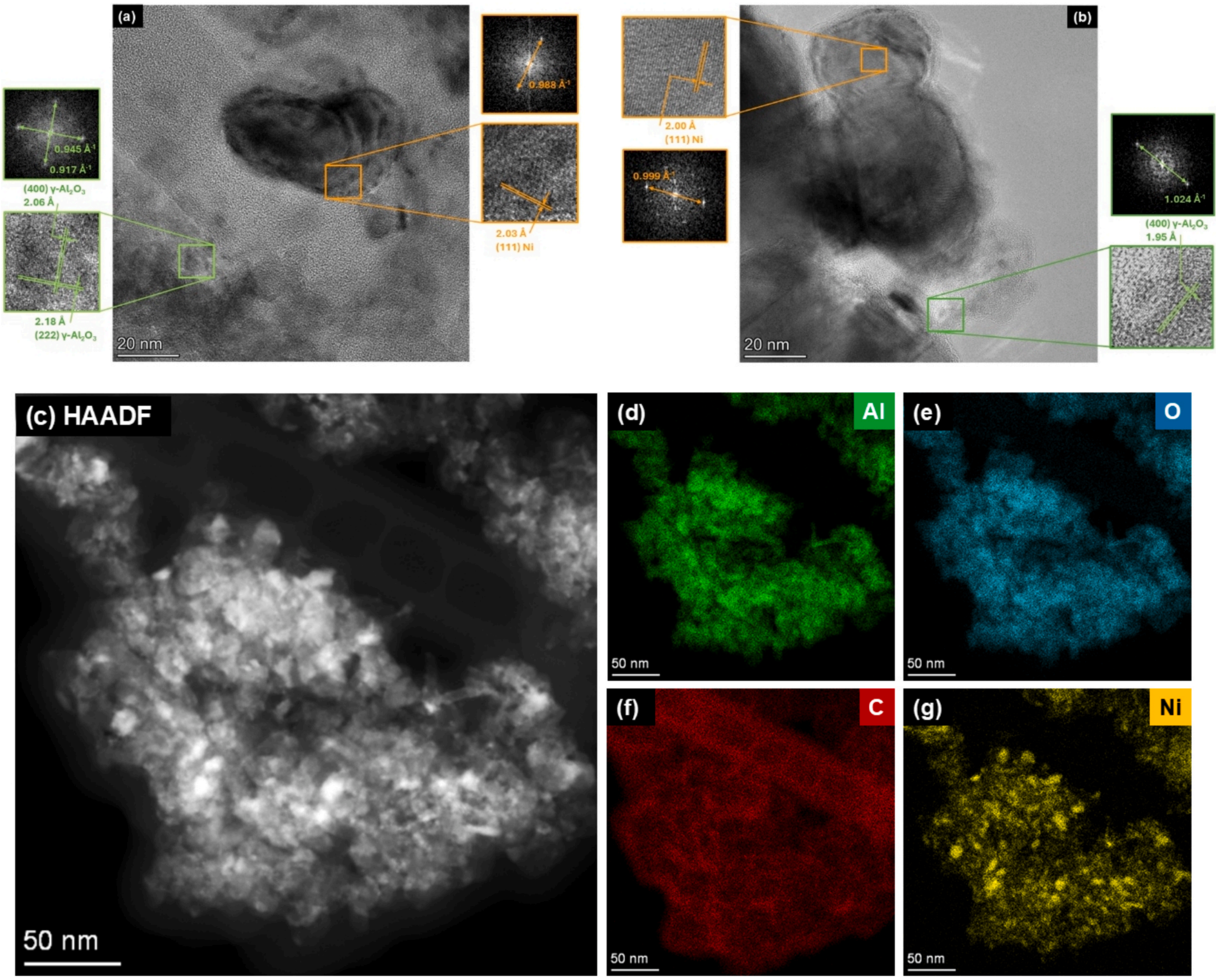

Fig. 4. (a, b) HR-TEM images of the reduced catalyst highlighting the fringes identified in the sample (magnification: (a) 500 kX and (b) 390 kX). (c) HAADF-STEM and (d-g) EDS maps of a particle of the reduced catalyst (magnification: 33 kX).

rates were experimentally observed with a very high over-stoichiometric H_2/CO ratio (i.e., 6.7 and 10), while it decreased with a H_2/CO ratio equal to 4. This may indicate an inhibiting effect of CO which competes with the H_2 adsorption and dissociation. Since CO adsorption is favored, a high CO concentration implies that most of the catalytic active sites are occupied by the CO* species and therefore H_2 struggles to adsorb.

Different effects of H_2 partial pressure were observed depending on the experiment (see Fig. S12). In group I, an increase of the H_2 partial pressure caused an increase of both the CH_4 yield and the CH_4 formation rate. In contrast, the effect of H_2 partial pressure is less evident in group II, where there were no significant changes in the CH_4 formation rate (see Fig. S13).

The effects of the CH_4 partial pressure were also investigated in group I and group II. The tests revealed that CH_4 behaves like an inert: an initial CH_4 concentration in the reactant mixture did not affect CO_2 and CO conversion. However, there may be deposition of solid carbon on the catalytic sites above 400 °C due to methane cracking reaction [9].

Lastly, the co-methanation of CO_2 and CO was also investigated on the catalyst. What stands out in Fig. 6 is that a competitive adsorption phenomenon was witnessed. The catalyst has been proved to have a greater affinity for CO, that preferentially adsorbs on the catalytic sites. By decreasing the CO concentration, the CO_2 adsorption and conversion did not improve, meaning that the competitive adsorption occurs also at low CO molar fraction (around 1.1 mol.%). As expected, CO conversion rose since it was not at equilibrium (Fig. 6.b). However, at low CO molar fraction (1.1 mol.%) the CO conversion progressively slowed down when CO started also to be formed by RWGS reaction at higher temperatures. Both the CH_4 formation rate (CO methanation reaction) and the CO formation rate (RWGS reaction) increased above 360 °C.

3.2.2. *Mass and heat transport criteria*

The mass and heat transport criteria were verified, and among all the 907 experimental observations, 22 of them did not meet the internal heat transport criterion (Anderson criterion), while the other three criteria (Mears criteria and Weisz-Prater criterion) were always verified. These 22 experimental trials, characterized by high reaction temperatures and conversions, were discarded from the simulation results.

3.2.3. *Power-law kinetic results*

Moving on now to the results obtained from the regression model using Power-law kinetics, parity plots for groups I and II are shown in Fig. 7. On the one hand, PL-CO2 and PL-HI kinetic models describe only the tests of group I, and specifically the CO_2 methanation and the RWGS reaction. On the other hand, PL-CO describes the CO methanation neglecting the WGS reaction. The kinetic parameters of the power-law models are given in Table 4, together with a confidence interval of 95 %.

Regarding the CO_2 methanation (group I), activation energies between 70 and 90 kJ/mol are reported in the literature by employing Ni/Al_2O_3 catalysts [20–22,42]. A slightly lower value, as in our case, may suggest higher catalyst activity. In the PL kinetic expression, n_{CO_2} is two orders of magnitude lower than n_{H_2}, highlighting the weak dependence on a change in CO_2 partial pressure. A kind of inhibitory effect by

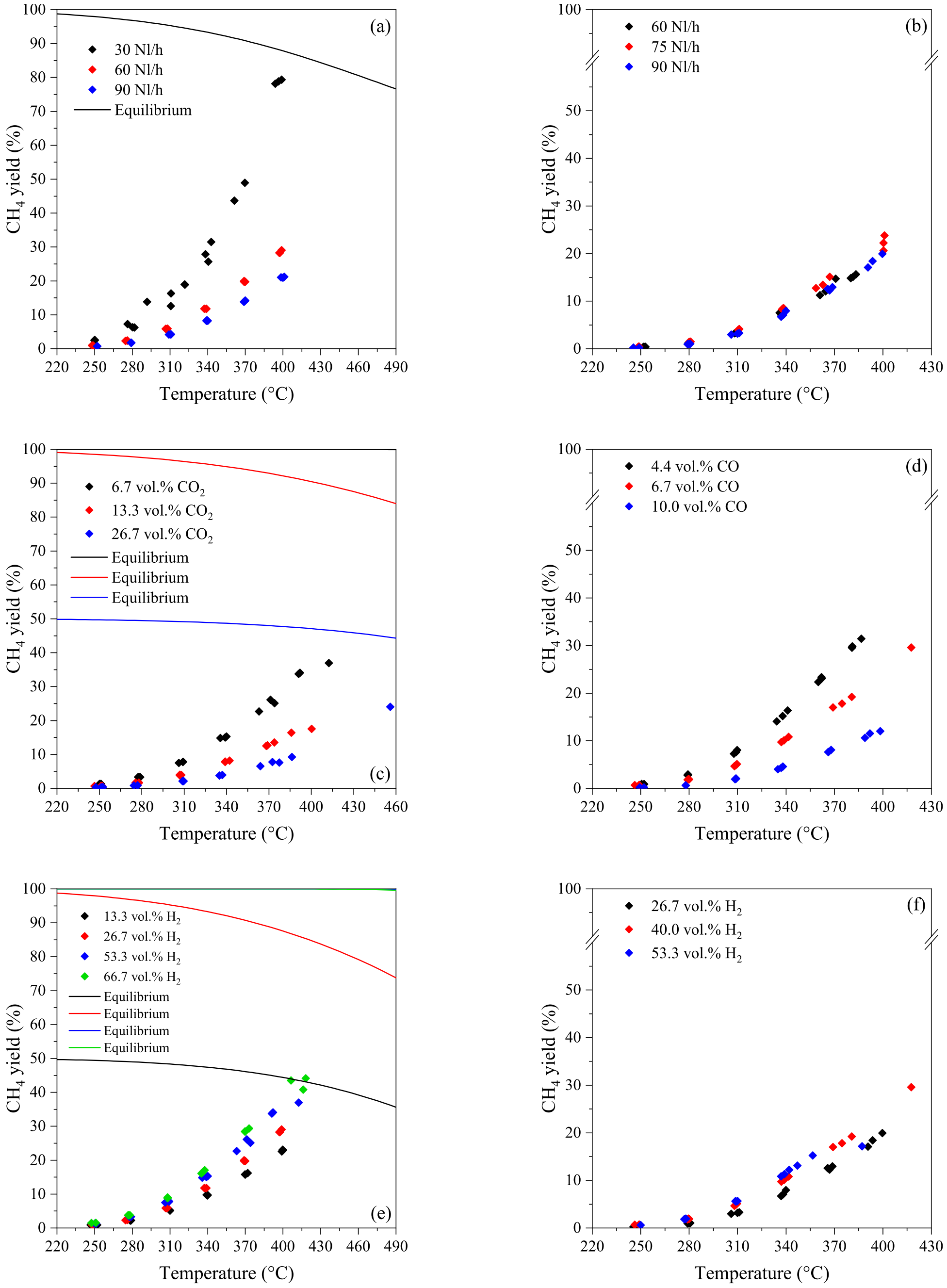

Fig. 5. CH_4 yield at 5 bar as temperature changes, considering the effect of: (a) residence time with mixture $CO_2/H_2/N_2 = 1/4/10$; (b) residence time with mixture $CO/H_2/N_2 = 1/4/10$; (c) CO_2 partial pressure with $CO_2/H_2/N_2$ gas mixture, flow rate 60 NL/h, H_2 molar fraction of 53.3 %; (d) CO partial pressure with $CO/H_2/N_2$ gas mixture, flow rate 90 NL/h, H_2 molar fraction of 40.0 %; (e) H_2 partial pressure with $CO_2/H_2/N_2$ gas mixture, flow rate 60 NL/h, CO_2 molar fraction of 6.7 %; (f) H_2 partial pressure with $CO/H_2/N_2$ gas mixture, flow rate 90 NL/h, CO molar fraction of 6.7 %.

hydrogen in RWGS reaction was also determined by Morosanu et al. [22] who found an inverse proportionality relationship between the CO formation and the H_2 partial pressure. It is worth noting that CO yield is about one order of magnitude lower than CH_4 yield because the desorption of CO is an unfavored process.

On the contrary, for the CO methanation reaction (group II), high CH_4 yields were not achieved to make thermal control easier and not end up at equilibrium. Although Power-law kinetics provide a good description of individual groups of reaction conditions, they could not be combined and are unable to describe CO_2 and CO co-methanation (group III) because of the competitive adsorption and the CO inhibitory effect.

3.2.4. LHHW kinetic results

As far as the proposed LHHW kinetic models (M1 to M5) are concerned, those that allow the experimental observations to be described are the models M2, M3, M4 and M5. Model M1 has been omitted from the following discussion, as it is already widely described in literature [20] and can only describe CO_2 methanation without considering the RWGS reaction. The reaction steps proposed by model M1 were taken for the derivation of model M4. Among all the 907 observations, 22 of them were excluded through the Anderson criterion, while 41 points were considered as outliers due to their high value of the Cook's distance [41]. Considering that 8 points did not verify both constraints, a total of 55 trials were discarded and 852 experimental observations were

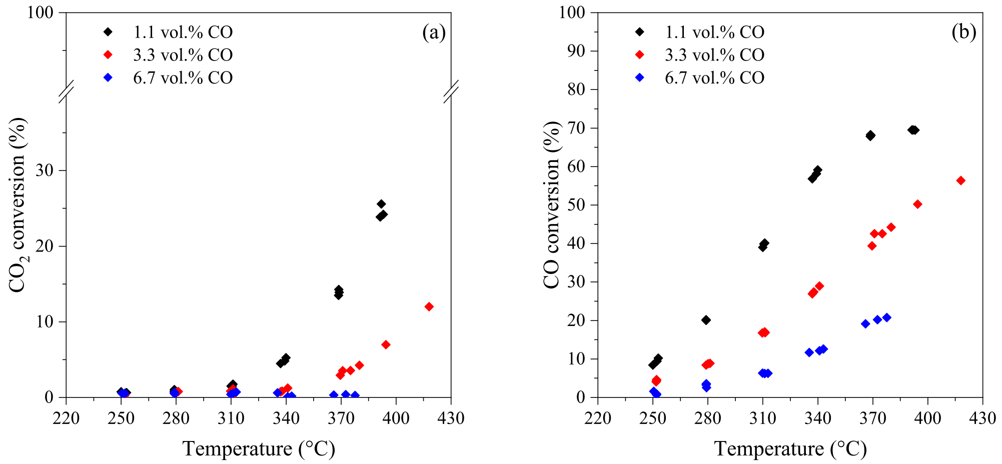

Fig. 6. CO_2 (a) and CO (b) conversion varying the CO partial pressure and the temperature by feeding 90 NL/h at 5 bar, 40.0 vol% H_2 and 3.3 vol% CO_2 in N_2.

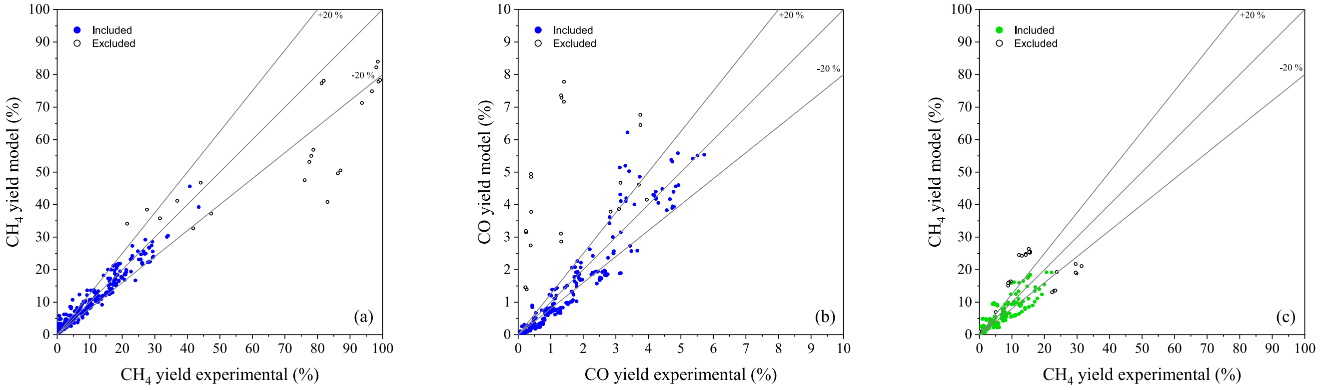

Fig. 7. Parity plots comparing experimental and modeled CH_4 yield (a) and CO yield (b) for group I (CO_2 methanation), and parity plot comparing the experimental and modeled CH_4 yield (c) for group II (CO methanation).

Table 4

Fitted kinetic parameters of the power law kinetic models assuming the reactor isothermal.

	CO_2 methanation (PL-CO2)	RWGS (PL-HI)	CO methanation (PL-COI)	Unit
k_{α,T_0}	$(1.32 \pm 0.01)\cdot 10^{-1}$	$(1.61 \pm 0.18)\cdot 10^{-2}$	$(3.33 \pm 0.30)\cdot 10^{-1}$	$molkg^{-1}s^{-1}bar^{-(n_{COx}+n_{H2})}$
$E_{A,\alpha}$	55.4 ± 0.3	105 ± 4	105 ± 7	$kJmol^{-1}$
$n_{CO_2,\alpha}$	$(5.20 \pm 2.06)\cdot 10^{-3}$	$(3.75 \pm 0.50)\cdot 10^{-1}$	–	–
$n_{H_2,\alpha}$	$(2.19 \pm 0.05)\cdot 10^{-1}$	3 ± 0.19	$(2.03 \pm 0.61)\cdot 10^{-1}$	–
$n_{CO,\alpha}$	–	–	$(4.18 \pm 1.46)\cdot 10^{-2}$	–
K_{H_2,T_0}	–	$(4.09 \pm 2.07)\cdot 10^{-3}$	–	bar^{-3}
ΔH_{H_2}	–	50.4 ± 7.6	–	$kJmol^{-1}$
K_{CO,T_0}	–	–	2.42 ± 0.17	$bar^{-0.042}$
ΔH_{CO}	–	–	50.9 ± 8.9	$kJmol^{-1}$

employed for the regression of the kinetic parameters of the four models.

The parity plots of the CH_4 yield obtained considering all experimental observations are reported in Fig. 8. Among the four models, model M4 allows a better description of the competitive adsorption phenomenon observed during the co-methanation of CO_2 and CO (group III) and of the influence of the operating pressure in the CO methanation tests (group II). This model fairly underestimates the experimental points near equilibrium; however, it provides a significantly better estimation of the results in the kinetic regime compared to models M2, M3 and M5. In more detail, the total sum of the quadratic residuals of the CH_4 yield was 1.094, 1.001, 0.972 and 0.806 for models M5, M2, M3 and M4, respectively. In addition, the standard deviation of the distributions of those residuals decreases from 0.0301 for model M5 to 0.0238 for model M4 as can be clearly observed in Fig. 8. Model M5 gave the worst results during the regression, meaning that the actual reaction mechanism is different from the one hypothesized. The average value of the residuals of the CH_4 yield is equal to 0.0236 for both M2 and M3 models, but the median value of model M3 (0.0155) is greater than the one of model M2 (0.0147). This may suggest that the mechanism of model M2 represents the different groups of tests better than model M3.

Lastly, the average value of the residuals of the CH_4 yield of model M4 resulted 0.0193 and the median value of their distribution was 0.0114. Hence, model M4 was considered the best kinetic model for representing the CO_2 and CO methanation on the Ni/Al_2O_3 catalyst under all reaction conditions. A more detailed comparison between models M3 and M4 is reported in Fig. S14 accentuating the attention on the three groups of operating conditions. Regarding CO_2 hydrogenation, model M4 fairly underestimates the CH_4 yield; however, it predicts

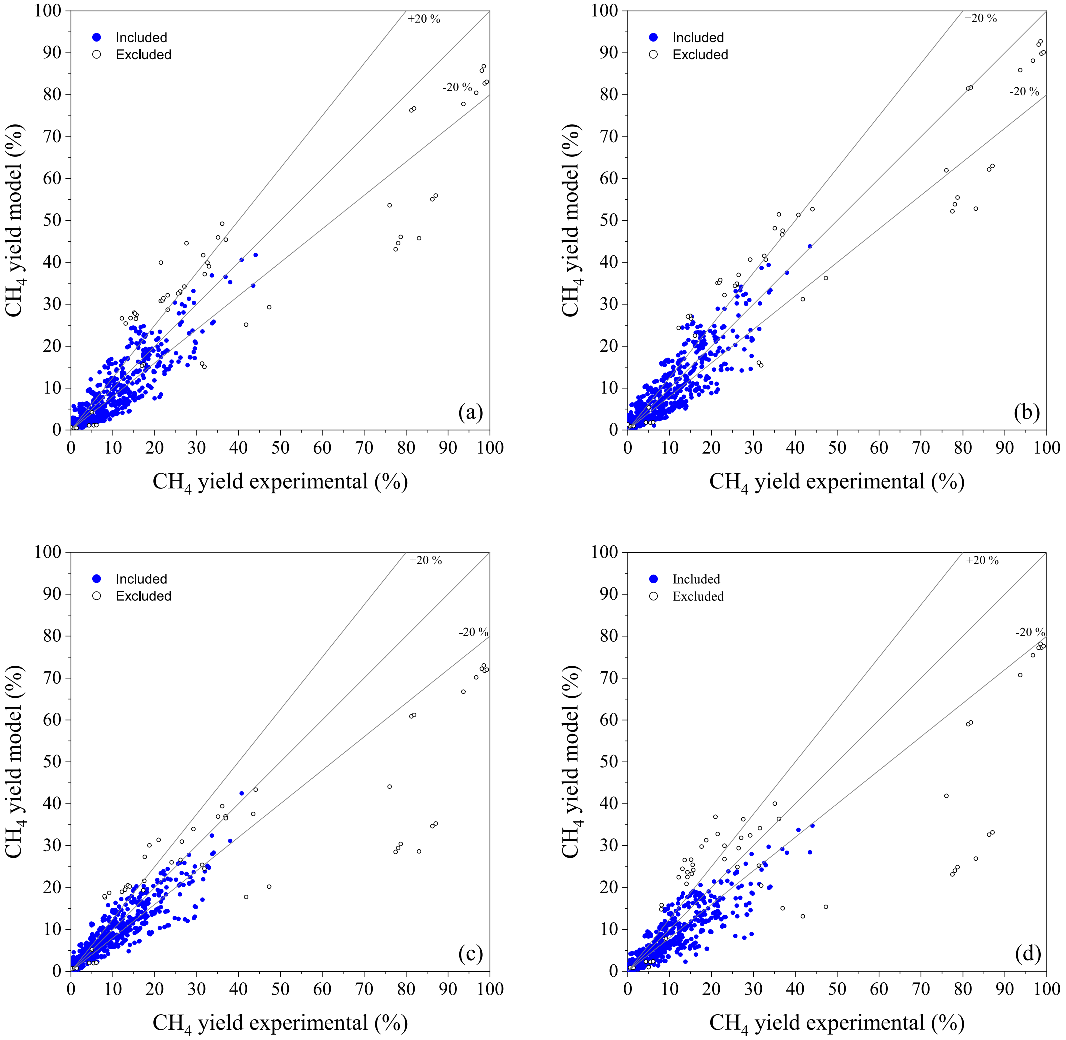

Fig. 8. Parity plots comparing experimental and modeled CH_4 yield obtained with models M2 (a), M3 (b), M4 (c) and M5 (d) considering the whole dataset.

significantly better the CO hydrogenation as well as the CO_2 and CO co-methanation processes. In fact, model M3 fails to accurately predict CH_4 yield, underestimating results at low pressure and overestimating those at high pressure. The accuracy of the different models in predicting the obtained results could help us draw some hypotheses on the prevailing mechanisms concerning the complex interplay between species in the investigated conditions of CO_2 methanation, CO methanation, CO_2 and CO co-methanation.

Based on the obtained results, CO_2 could adsorb either associatively by forming COOH* or dissociatively by forming CO* and O*. Moreover, CO* was chosen as the reaction intermediate for both CO_2 and CO methanation as it is the most thermodynamically favored species on the surface of Ni sites [14]. It was assumed that CO_2 converts first to CO via RWGS reaction and then CH_4 formation occurs through hydrogenation of CO* species. Different mechanisms for CO_2 adsorption and CO* hydrogenation to CH* have been considered depending on several aspects: concentration of CO_2 and H_2, reaction conditions, availability of active sites and surface species. According to the literature, Quindimil et al. [26] have proposed the H-assisted CO formation mechanism. CO_2 is molecularly chemisorbed on superficial –OH groups of Al_2O_3 support forming bicarbonates (HCO_3*). After that, bicarbonates react with dissociated H_2 leading to the formation of formate species (HCOO*) which are decomposed into OH* and CO*. Then carbonyl groups can desorb from the catalytic surface releasing CO, or they can be hydrogenated leading to the formation of CH_4.

On the one hand, considering only CO_2 hydrogenation experiments (group I), an inhibiting effect of H* species was present, suggesting that the H-assisted associative CO_2 adsorption mechanism should be preferred with respect to the dissociative CO_2 adsorption mechanism, which requires two free active sites. Hence, under these reaction conditions, the concentration of H* species is greater than the concentration of CO* species favoring all hydrogenation reactions. Moreover, no hydrocarbons were detected by the GC in any tests of group I and, as it will be presented in the following paragraphs, the catalyst did not seem to be affected by coking during CO_2 methanation. Therefore, it is likely that, with the composition adopted for the experiments, CO* is hydrogenated forming a formyl (HCO*) species before dissociating into CH* and O*, instead of decomposing and forming C* species.

On the other hand, if the partial pressure of CO is high, as for the CO hydrogenation tests (group II) or for the CO_2 and CO co-methanation tests (group III), CO* is expected to be the most abundant species on the catalyst surface due to the exergonic CO adsorption process. This phenomenon explains both the inhibiting effect of CO and the competitive adsorption process observed varying the reaction conditions. The high CO* coverage probably competes also with the H_2 adsorption process, limiting H* coverage. Hence, the abundance of superficial CO* species favors the dissociative carbon pathway leading to the formation of C* species. Consequently, as explained in the next paragraphs, C* led to the formation of nickel carbides and coking.

In conclusion model M4 can describe all the mentioned phenomena, and the kinetic parameters are given in Table 5 together with the kinetic parameters obtained for models M2 and M3. The confidence interval is 95 % and the thermodynamic constrains ($0 \le K_{i,T_0} \le \exp\left(\frac{\Delta \widetilde{S}^0_{i,T_0}}{R}\right)$) on the pre-exponential factor of the van't Hoff expression have been always verified for all adsorbed species.

A sensitivity analysis on the kinetic parameters of model M4 was performed to illustrate the influence of the kinetic parameters on the objective function. As shown in Fig. S15, it is significantly affected by the kinetic parameters of the CO_2 methanation and moderately affected by those describing RWGS reaction and CO methanation. Regarding the adsorption group, the objective function is mainly affected by the pre-exponential factor related to the H_2 adsorption term. These results are consistent with those in the literature [22]. Lastly, Fig. 9 shows the parity plots for model M4 of the molar fractions of CO_2, CO, CH_4 and H_2 exiting the reactor. What stands out from the figure is that there is a strict correlation between the experimental and the modeled molar fractions. The highest inaccuracy is linked to the measurement of H_2 concentration because helium is used as carrier gas in the GC and the sensibility of the TCD is slightly lower. However, the gas analyzer was used to double-check its concentration in the gas stream.

3.3. *Stability and deactivation results*

So far, this article focused on the modelling of the intrinsic kinetics of CO and CO_2 hydrogenation to methane over the 24 wt% Ni/Al_2O_3 catalyst. The following section will discuss the results of the deactivation tests performed on this catalyst to evaluate its resistance to temperature, gas composition and contaminants that could be present in the feed. Moreover, Power-Law kinetics models of the deactivation will be presented and discussed. Biogas-derived CO_2 or pyro-gas from pyrolysis or gasification may contain traces of light hydrocarbons (e.g., ethylene), O_2 and H_2S; thus, their effects were investigated. As previously stated, the operative conditions of the stability tests are summarized in Table S4.

3.3.1. *H_2S poisoning effect*

As far as the sulfur poisoning effect is concerned, an adsorption test with 200 ppm H_2S/CH_4 on the pre-reduced catalyst was performed. After that, the comparison between the activity of the fresh and H_2S-poisoned catalysts allowed the total number of active sites, the Ni particle size and the Ni dispersion to be estimated. Then the residual activity was measured. As shown in Fig. 10, an exposure to 200 ppm H_2S/CH_4 for 160 min is sufficient to almost completely poison the catalyst, which exhibited a residual CO_2 conversion lower than 5 % at 400 °C. The deactivation occurred because H_2S binds on the active sites of the catalyst according to the reaction reported in equation (29).

$$H_2S + Ni \rightleftharpoons Ni - S + H_2 \tag{29}$$

As summarized in Table 6, during the H_2S adsorption test, 164 mmol kg^{-1} of H_2S were adsorbed, so considering the residual activity of the catalyst, the total concentration of active sites is 175 mmol kg^{-1}.

Moreover, according to equation (30), the Ni dispersion in the fresh pre-reduced catalyst resulted equal to 4.3 %; while according to equation (31), the volume-area mean diameter of the Ni particles in the fresh pre-reduced catalyst is about 25 nm.

$$D_{Ni} = \frac{N_{s,Ni}}{N_{t,Ni}} = N_{s,Ni} \cdot \frac{M_{Ni}}{w_{Ni}} \tag{30}$$

$$d_{VA,Ni} = \frac{6 \cdot v_{m,Ni}}{D_{Ni} \cdot a_{m,Ni}} = \frac{6}{D_{Ni}} \cdot \frac{M_{Ni}}{\rho_{Ni} \cdot N_A} \cdot \frac{n_{Ni}}{a^2_{Ni}} \tag{31}$$

Analyzing the elemental composition of the H_2S poisoned catalyst, the EDS measurement (Fig. S16) revealed that sulfur is uniformly present on the surface of the catalyst (0.3 wt%). Due to the small amount of adsorbed sulfur, the XRD measurement (see Fig. S6) did not reveal the presence of NiS.

3.3.2. *CO_2 hydrogenation*

Starting from the first group of stability tests (i.e., ST1, ST2 and ST3), the deactivation rate of the catalyst at different reaction temperatures (i.e., 425 °C, 350 °C and 470 °C, respectively) was analyzed. The gas mixture was kept stoichiometric or slightly over-stoichiometric to avoid carbon deposition that, according to the literature, does not occur in CO_2 methanation [22,30]. Fig. 11 illustrates the time-on-stream profile of the CO_2 conversion of the three tests; as expected, it is higher at elevated temperatures, and it decreases over time with a deactivation rate accelerating at higher temperatures. During the tests as the CO_2 conversion diminished, the CO selectivity increased as well as the temperature rose because RWGS reaction is favored at high temperatures.

Activity tests performed before and after the stability tests revealed a change in the activity that is mainly related to a reduction of active sites and not to the change of the reaction mechanism. Therefore, the deac-

Table 5
Fitted parameters for the LHHW kinetic models (M2, M3, M4, M5) considering the whole dataset.

Parameter	Unit	Model M2	Model M3	Model M4	Model M5
k_{1,T_0}	$molkg^{-1}s^{-1}bar^{-1.5}$	–	–	$(1.68 \pm 0.36) \cdot 10^{-2}$	$(3.87 \pm 0.27) \cdot 10^{-1}$
k_{2,T_0}	$molkg^{-1}s^{-1}bar^{-1.5}$	42.6 ± 0.3	51.4 ± 1.1	1.50 ± 0.01	1.50 ± 0.01
k_{3,T_0}	$molkg^{-1}s^{-1}bar^{-1.5}$	$(9.43 \pm 0.57) \cdot 10^{-1}$	1.45 ± 0.05	$(1.19 \pm 0.08) \cdot 10^{-1}$	$(3.08 \pm 0.44) \cdot 10^{-1}$(a)
$E_{A,1}$	$kJ \cdot mol^{-1}$	–	–	118 ± 4	91.0 ± 5.0
$E_{A,2}$	$kJ \cdot mol^{-1}$	22.2 ± 0.4	44.3 ± 1.9	54.9 ± 1.4	65.4 ± 5.4
$E_{A,3}$	$kJ \cdot mol^{-1}$	87.4 ± 2.0	88.5 ± 1.2	110 ± 3	93.8 ± 7.7
K_{H_2,T_0}	bar^{-1}	$(1.82 \pm 0.11) \cdot 10^{-1}$	$(3.17 \pm 0.22) \cdot 10^{-1}$	$(5.00 \pm 0.01) \cdot 10^{-1}$	$(1.71 \pm 0.15) \cdot 10^{-1}$
ΔH_{H_2}	$kJ \cdot mol^{-1}$	-3.25 ± 0.29	-7.93 ± 2.42	-8.76 ± 0.20	-6.88 ± 0.16
K_{COOH,T_0}	$bar^{-1.5}$	$(9.76 \pm 1.50) \cdot 10^{-2}$	–	–	–
ΔH_{COOH}	$kJ \cdot mol^{-1}$	-3.95 ± 0.34	–	–	–
K_{OH,T_0}	$bar^{-0.5}$	$(4.07 \pm 0.39) \cdot 10^{-2}$	–	–	–
ΔH_{OH}	$kJ \cdot mol^{-1}$	-51.4 ± 0.4	–	–	–
K_{CO,T_0}	bar^{-1}	41.3 ± 0.2	40.0 ± 0.01	1.41 ± 0.04	2.45 ± 0.19
ΔH_{CO}	$kJ \cdot mol^{-1}$	-25.7 ± 0.5	-5.76 ± 1.54	-38.5 ± 0.9	-16.2 ± 0.84
K_{C,T_0}	bar^{1}	–	$(1.99 \pm 0.01) \cdot 10^{-1}$	1.78 ± 0.09	–
ΔH_{C}	$kJ \cdot mol^{-1}$	–	-28.5 ± 4.0	-20.0 ± 0.7	–
K_{CH_4,T_0}	bar^{-1}	–	$(3.09 \pm 0.09) \cdot 10^{-1}$	$(5.00 \pm 0.01) \cdot 10^{-1}$	$(6.77 \pm 1.32) \cdot 10^{-2}$
ΔH_{CH_4}	$kJ \cdot mol^{-1}$	–	12.6 ± 0.2	18.8 ± 0.4	40.9 ± 2.4
K_{H_2O,T_0}	–	–	–	–	16.8 ± 3.2
ΔH_{H_2O}	$kJ \cdot mol^{-1}$	–	–	–	-30.5 ± 0.7

(a) The unit is $mol \cdot kg^{-1} \cdot s^{-1} \cdot bar^{-1}$

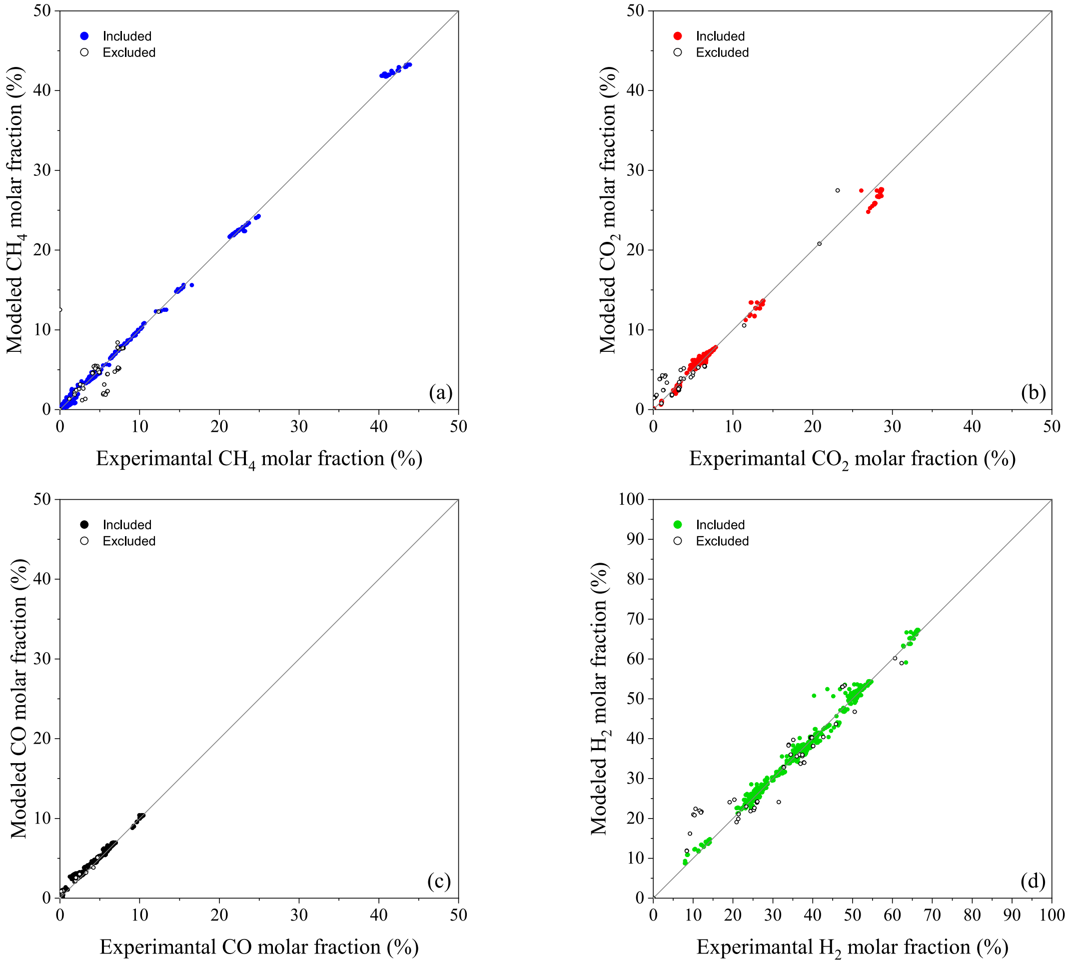

Fig. 9. Parity plots for model M4 comparing the experimental and the modeled molar fractions at the reactor outlet for the following gas species: (a) CH_4, (b) CO_2 (c) CO and (d) H_2.

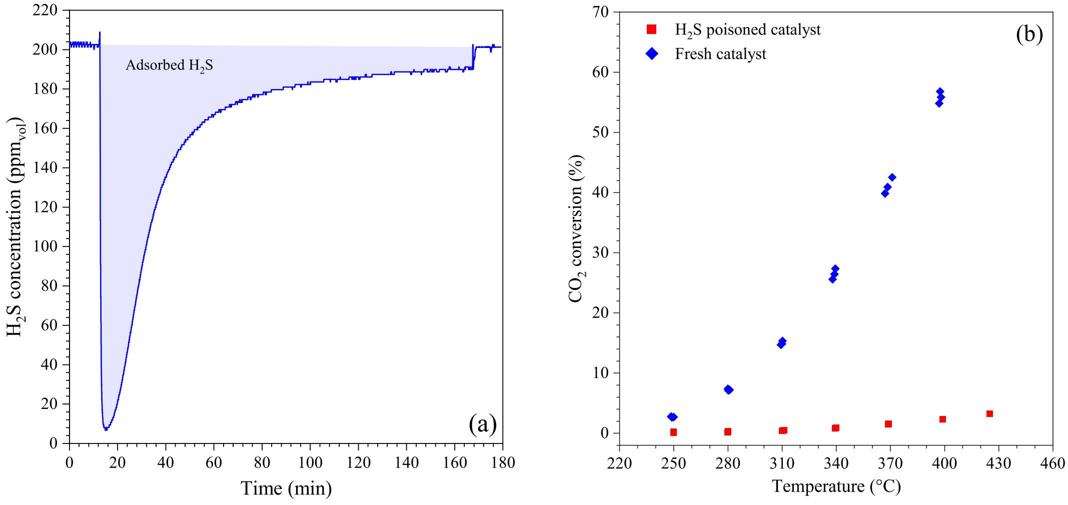

Fig. 10. (a) H_2S adsorption profile on 450 mg Ni/Al_2O_3 catalyst (Conditions: 15 NL/h, 1 bar, 20 °C, 200 ppm H_2S/CH_4) and (b) CO_2 conversion at different reaction temperatures of the fresh pre-reduced and H_2S-poisoned catalysts (Conditions: 75 mg of catalyst, 350 mg SiC, 60 NL/h, 5 bar, $H_2/CO_2/N_2 = 4/1/25$).

tivation was ascribed to thermal sintering that causes a reduction of the exposed Ni surface area and structural changes, as can be clearly seen from the SEM images in Fig. S17. In fact, by estimating the average mean diameter of Ni particles according to equations (31) and (32), it increased from 25 nm for the fresh pre-reduced catalyst to 27.3 nm, 33.4 nm and 36.2 nm for the deactivated catalyst at 350 °C, 425 °C and 470 °C, respectively.

$$d_{VA,spent} = d_{VA,fresh} \cdot \frac{k_{T_0,fresh}}{k_{T_0,spent}} \tag{32}$$

Table 6

Comparison between the characteristics of the reduced and the H_2S-poisoned catalysts, by assuming a simple 1st order reaction rate for the CO_2 methanation reaction.

Material	k_{T_0}	E_A	Active sites
	mol s^{-1} kg^{-1}	kJ mol^{-1}	mmol kg^{-1}
Fresh pre-reduced catalyst	$5.85 \cdot 10^{-2}$	40.7	175
H_2S-poisoned catalyst	$3.90 \cdot 10^{-3}$	40.7	11

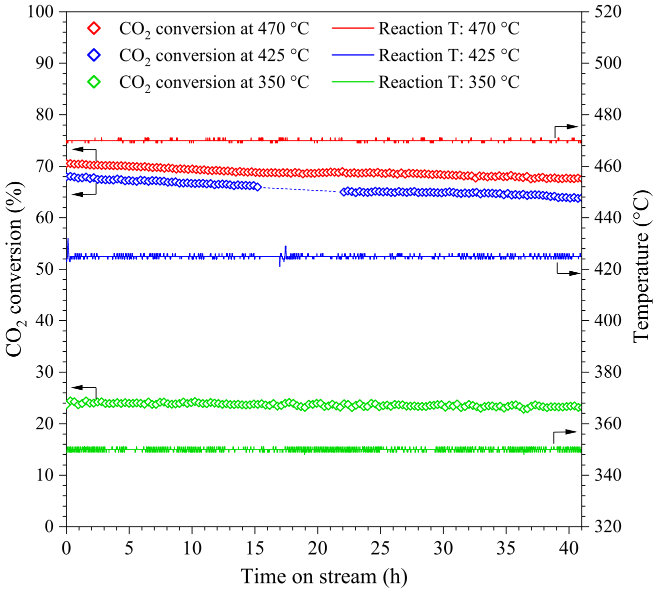

Fig. 11. Time-on-stream profile of the CO_2 conversion at different reaction temperatures by feeding 60 NL/h at 5 bar with composition $H_2/CO_2/N_2 = 4/1/25$.

The deactivation rate under these three reaction conditions was described by means of equation (33) considering both the effect of H_2 and CO_2 concentration, that could be related to the H* or OH* and CO* adsorbed species, respectively.

$$\frac{da}{dt} = -k_{d,1,T_0} \cdot \exp\left[\frac{-E_{d,1}}{R} \cdot \left(\frac{1}{T} - \frac{1}{T_0}\right)\right] \cdot C_{H_2}^{q_{H_2,1}} \cdot C_{CO_2}^{q_{CO_2,1}} \cdot a^d \tag{33}$$

As can be seen in Table 7, the pre-exponential factor ($k_{d,1,T_0}$) and the activation energy for sintering ($E_{d,1}$) are both lower than those reported in the literature [22,27,30], meaning that the catalyst exhibited a good resistance to thermal sintering. In addition, the deactivation order (d) is significantly lower than those available in the literature [22,30], suggesting that the pre-treatment of the Ni/Al_2O_3 catalyst under H_2 stabilized its structure without losing performance. Lastly, sintering is promoted by a higher concentration of H_2 ($q_{H_2,1} > 0$), while it is mitigated by the addition of CO_2 ($q_{CO_2,1} < 0$). X-ray data (see Fig. S6) indeed indicate incomplete reduction of NiO, suggesting that H₂ also drives a gradual structural rearrangement occurring during the test. However, under-stoichiometric gas mixtures were not investigated due to coking, that was not modelled under these reaction conditions.

3.3.3. CO hydrogenation

Moving on now to consider the effects of a CO/H_2 gas mixture, three different conditions were explored. As can be seen in Fig. 12a, considering an over-stoichiometric gas mixture (H_2/CO equal to 4), severe deactivation occurs at low temperature, that was ascribed to the formation of nickel carbides on the surface of the catalyst. Nickel carbides are active for the Fischer-Tropsch process and produce a lot of hydrocarbons lowering the methane selectivity [27]. According to the previous results, as CO adsorption is an extremely favored process, the high CO* coverage improves the CO* dissociation forming C* species. Thus, C* species could diffuse in the nickel structure allowing nickel carbide to be formed instead of being hydrogenated into CH* species. By rising the temperature, the CO adsorption process is unfavored and the CO* coverage diminishes; as a result, methane is the most important product of the reaction and ethane is the only by-product, as can be seen in Fig. S18. On the contrary, in Fig. 12b, the stability of the catalyst was tested at stoichiometric H_2/CO ratio equal to 3. This one was the worst operative condition due to a dramatic decline of the catalytic activity, meaning that the coking predominates and severely affects the catalyst reducing the concentration of H* species. Concerning the deactivation rate expression (see equation (34)), the apparent energy of activation for coking is negative, thus a higher temperature mitigates carbon deposition while it accelerates thermal sintering. Moreover, the exponents of H_2 and CO concentrations are both positive revealing a strong instability of the catalyst under such reducing atmospheres.

$$\frac{da}{dt} = -k_{d,2,T_0} \cdot \exp\left[\frac{-E_{d,2}}{R} \cdot \left(\frac{1}{T} - \frac{1}{T_0}\right)\right] \cdot C_{H_2}^{q_{H_2,2}} \cdot C_{CO}^{q_{CO,2}} \cdot a^d \tag{34}$$

The sample aged at 330 °C was characterized to investigate in more detail the causes of deactivation. Sintering phenomena occurred under reaction conditions as can be seen from SEM images reported in Fig. S19. In addition, EDS showed that carbon is uniformly present on the surface of the sample. However, the diffractogram of the sample (Fig. S6) did not reveal the presence of nickel carbides. There are three possible explanations to this fact: (i) the amount of nickel carbides is below the XRD detection limit (< 5 wt%), (ii) nickel carbides formed an amorphous phase or (iii) they decomposed during the activity test performed to verify the residual activity of the sample after the stability test. The latter seems to be the most plausible reason as nickel carbide (Ni_3C) decomposes rapidly in H_2-rich and CO-poor environments above 350 °C [43,44].

3.3.4. CO and CO_2 co-methanation

Besides the previous cases of study, the stability of the catalyst under CO-CO_2 co-methanation conditions was investigated by varying the

Table 7

Fitted kinetic parameters of the deactivation rate assuming the reactor isothermal.

Parameter	Unit	Value	Parameter	Unit	Value
$k_{d,1,T_0}$	$\frac{1}{s} \cdot \left(\frac{m^3}{mol}\right)^{q_{H_2,1}+q_{CO_2,1}}$	$(1.16 \pm 0.15) \cdot 10^{-7}$	$q_{H_2,1}$	–	0.49 ± 0.12
$k_{d,2,T_0}$	$\frac{1}{s} \cdot \left(\frac{m^3}{mol}\right)^{q_{H_2,2}+q_{CO,2}}$	$(9.87 \pm 0.26) \cdot 10^{-7}$	$q_{CO_2,1}$	–	-0.39 ± 0.32
$k_{d,3,T_0}$	$\frac{1}{s} \cdot \left(\frac{m^3}{mol}\right)^{q_{H_2,1}+q_{CO_2,1}+q_{H_2,2}+q_{CO,2}}$	$(3.50 \pm 0.75) \cdot 10^{-10}$	$q_{H_2,2}$	–	2.47 ± 0.14
$E_{d,1}$	$kJ \cdot mol^{-1}$	35.4 ± 4.5	$q_{CO,2}$	–	2.88 ± 0.43
$E_{d,2}$	$kJ \cdot mol^{-1}$	-21.3 ± 1.6	$q_{C_2H_4}$	–	9.34 ± 0.05
$E_{d,3}$	$kJ \cdot mol^{-1}$	131 ± 12	q_{O_2}	–	3.59 ± 0.11
d	–	5.14 ± 0.05			

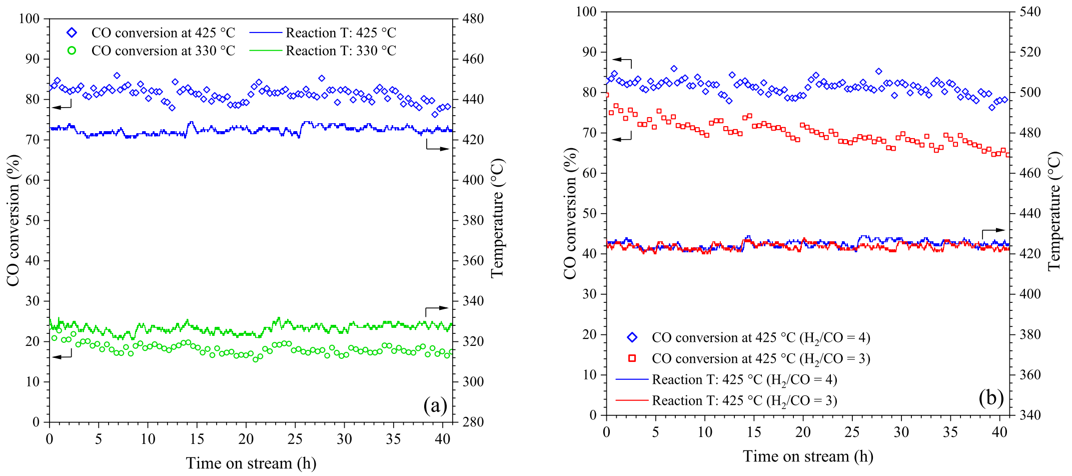

Fig. 12. Time-on-stream profiles of the CO conversion at different reaction temperatures by feeding 60 NL/h at 5 bar, varying the temperature (a) or the gas composition (b). For the sake of clarity, in figure (a) the composition is $H_2/CO/N_2 = 4/1/25$ and the temperature is 330 °C (green) or 425 °C (blue); while in figure (b) the temperature is 425 °C and the two gas compositions are $H_2/CO/N_2 = 4/1/25$ (blue) and $H_2/CO/N_2 = 3/1/25$ (red). (For interpretation of the references to colour in this figure legend, the reader is referred to the web version of this article.)

reaction temperature. As displayed in Fig. 13, both CO and CO_2 conversions increased when rising the temperature and the CO conversion remained always above the CO_2 conversion, indicating a preferential adsorption of CO on the catalytic sites compared to CO_2. Therefore, the catalytic deactivation phenomena are comparable with the CO hydrogenation tests. However, the presence of CO_2 seems to partially mitigate deactivation, in fact, at low temperature (350 °C), only a small concentration of ethane (40 ppm) was detected as a byproduct and no heavier hydrocarbons were noticed. The deactivation rate (see Eq. (35)) remained quite high and became more significant by increasing the temperature and the H_2 and CO concentrations.

$$\frac{da}{dt} = -k_{d,3,T_0}\cdot\exp\left[\frac{-E_{d,3}}{R}\cdot\left(\frac{1}{T}-\frac{1}{T_0}\right)\right]\cdot C_{H_2}^{q_{H_2,1}+q_{H_2,2}}\cdot C_{CO_2}^{q_{CO_2,1}}\cdot C_{CO}^{q_{CO,2}}\cdot a^d \qquad (35)$$

3.3.5. O_2 and ethylene effects

Light hydrocarbons, such as ethylene (C_2H_4), and O_2 could be possible contaminants present in pyro-gas deriving from pyrolysis or gasification that could deactivate the methanation catalyst. As can be clearly seen in Fig. 14, both ethylene and O_2 worsened the stability of the catalyst. On the one hand, ethylene was used as probe molecule to study the effects of light reactive hydrocarbons. It is worth noting that the deactivation rate (see Eq. (36)) slightly increased in the presence of 800 ppm of C_2H_4. Under reaction condition ethylene was completely converted to ethane (39 %) and methane (61 %). The additional deactivation phenomenon was ascribed to the ethylene decomposition into methane and solid carbon that caused coking [19]. On the other hand, O_2 presence (1400 ppm) led to an additional deactivation phenomenon that was ascribed to highly exothermic hydrogenation of O_2 to water, which favored the sintering process (see Eq. (37)). Hence, the concentration of both contaminants should be minimized to preserve the activity of the catalyst.

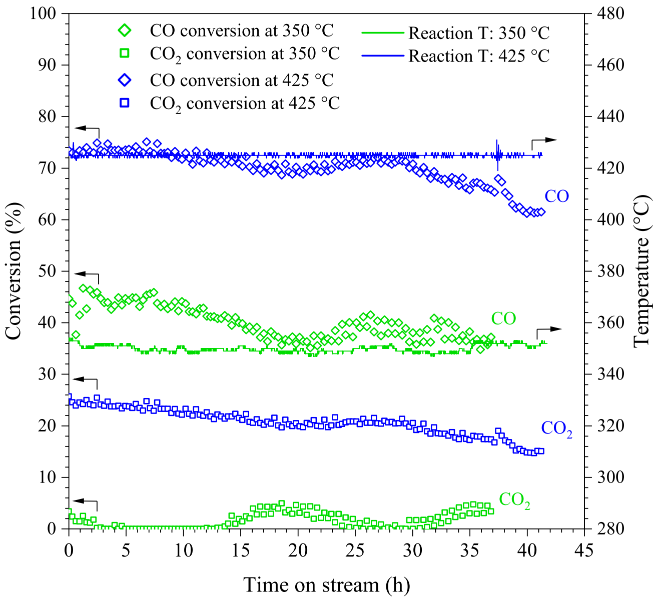

Fig. 13. Time-on-stream profiles of both CO and CO_2 conversion during co-methanation at two reaction temperatures (350 °C and 425 °C) by feeding 60 NL/h at 5 bar with a gas composition equal to $H_2/CO/CO_2/N_2 = 8/1/1/50$.

$$\frac{da}{dt} = -k_{d,1,T_0}\cdot\exp\left[\frac{-E_{d,1}}{R}\cdot\left(\frac{1}{T}-\frac{1}{T_0}\right)\right]\cdot C_{H_2}^{q_{H_2,1}}\cdot C_{CO_2}^{q_{CO_2,1}}\cdot\left(1+C_{C_2H_4,in}\right)^{q_{C_2H_4}}\cdot a^d \qquad (36)$$

$$\frac{da}{dt} = -k_{d,1,T_0}\cdot\exp\left[\frac{-E_{d,1}}{R}\cdot\left(\frac{1}{T}-\frac{1}{T_0}\right)\right]\cdot C_{H_2}^{q_{H_2,1}}\cdot C_{CO_2}^{q_{CO_2,1}}\cdot\left(1+C_{O_2,in}\right)^{q_{O_2}}\cdot a^d \qquad (37)$$

3.3.6. Deactivation rate parameters

In Table 7 are summarized all the parameters fitted for the deactivation rates with a confidence interval of 95 %. In addition, Fig. S20 displays the comparison between the experimental and modeled activity for all the ten deactivation tests presented in the previous paragraphs. It is worth highlighting that the observed evolutions of the activity in Fig. S20 are affected not only by the mentioned temperature-related deactivation mechanisms, but they also depend on the different reactant concentrations during the tests, which affected by the temperature as well.

3.3.7. Operative map

From a pragmatic point of view, the results of the deactivation tests and of the simulations could be summarized in an operative map highlighting the deactivation constants for a simple 1st order deactivation rate, that can be used to set boundaries on the operative conditions to minimize catalyst deactivation. As can be seen in Fig. 15, it is worth noting that in CO_2 methanation the catalyst degradation is minor below 350 °C, while above this temperature the deactivation is increasingly

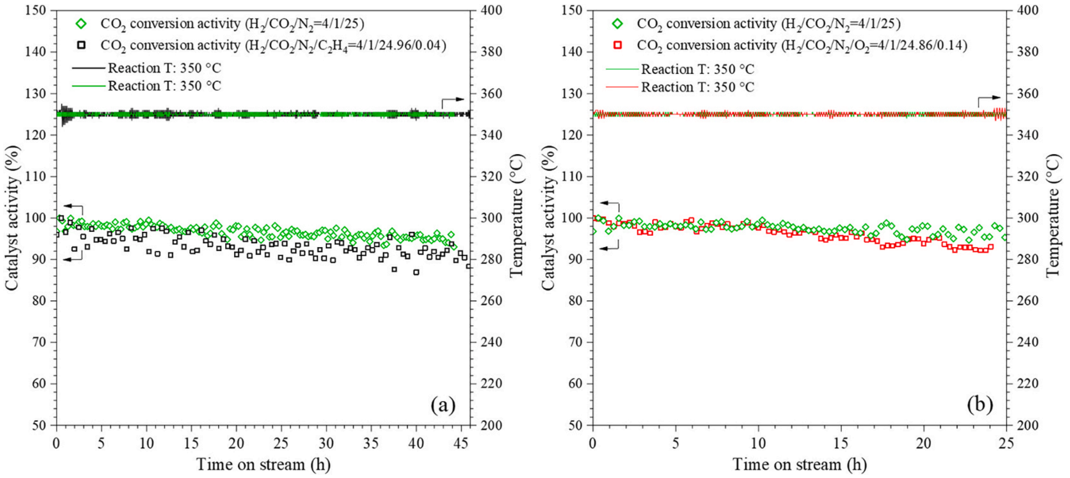

Fig. 14. Time-on-stream profiles of the activity of the Ni/Al_2O_3 catalyst at two different reaction temperatures by feeding 60 NL/h at 5 bar considering (a) C_2H_4 contamination ($H_2/CO_2/N_2/C_2H_4 = 4/1/24.96/0.04$) and (b) O_2 contamination ($H_2/CO_2/N_2/O_2 = 4/1/24.86/0.14$). For the sake of clarity, the gas composition of the reference test was ($H_2/CO_2/N_2 = 4/1/25$).

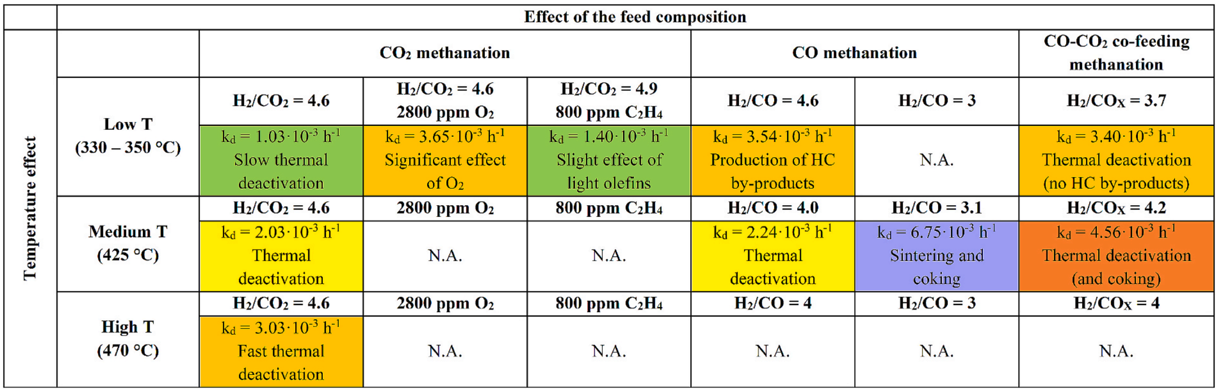

		Effect of the feed composition					
		CO₂ methanation			CO methanation		CO-CO₂ co-feeding methanation
Temperature effect	Low T (330 – 350 °C)	$H_2/CO_2 = 4.6$ $k_d = 1.03\cdot10^{-3}$ h⁻¹ Slow thermal deactivation	$H_2/CO_2 = 4.6$ 2800 ppm O_2 $k_d = 3.65\cdot10^{-3}$ h⁻¹ Significant effect of O_2	$H_2/CO_2 = 4.9$ 800 ppm C_2H_4 $k_d = 1.40\cdot10^{-3}$ h⁻¹ Slight effect of light olefins	$H_2/CO = 4.6$ $k_d = 3.54\cdot10^{-3}$ h⁻¹ Production of HC by-products	$H_2/CO = 3$ N.A.	$H_2/CO_X = 3.7$ $k_d = 3.40\cdot10^{-3}$ h⁻¹ Thermal deactivation (no HC by-products)
	Medium T (425 °C)	$H_2/CO_2 = 4.6$ $k_d = 2.03\cdot10^{-3}$ h⁻¹ Thermal deactivation	2800 ppm O_2 N.A.	800 ppm C_2H_4 N.A.	$H_2/CO = 4.0$ $k_d = 2.24\cdot10^{-3}$ h⁻¹ Thermal deactivation	$H_2/CO = 3.1$ $k_d = 6.75\cdot10^{-3}$ h⁻¹ Sintering and coking	$H_2/CO_X = 4.2$ $k_d = 4.56\cdot10^{-3}$ h⁻¹ Thermal deactivation (and coking)
	High T (470 °C)	$H_2/CO_2 = 4.6$ $k_d = 3.03\cdot10^{-3}$ h⁻¹ Fast thermal deactivation	2800 ppm O_2 N.A.	800 ppm C_2H_4 N.A.	$H_2/CO = 4$ N.A.	$H_2/CO = 3$ N.A.	$H_2/CO_X = 4$ N.A.

Fig. 15. Operative map summarizing the deactivation rates.

relevant. This suggests limiting the hot spots in full-scale reactors. On the contrary, in CO hydrogenation, not necessarily the lowest temperatures are better, since some by-products (hydrocarbons from C_2 to C_5) form at 350 °C while are negligible at 425 °C. Moreover, over-stoichiometric H_2/CO ratios improve considerably the stability of the catalyst with respect to stoichiometric ones, for which coke formation occurs in addition to thermal degradation, leading to a relatively fast deactivation. This suggests performing CO methanation at medium temperatures (around 425 °C) and over-stoichiometric H_2/CO ratios to preserve the catalyst from fast sintering and coking. In the third configuration, the co-feeding of CO_2 in CO methanation avoids the formation of heavier hydrocarbons at low temperatures, but the catalyst deactivates faster as the temperature increases. Also in this case, an over-stoichiometric $H_2/(CO + CO_2)$ ratio is recommended to minimize coking.

As far as contaminants are concerned, the effects of O_2 and light olefins (C_2H_4) have been investigated. The presence of O_2 is detrimental for the catalyst since its hydrogenation is highly exothermic and presumably worsens the thermal degradation; thus, its concentration should be minimized. Whereas, ethylene leads to a minor additional deactivation, so as low as possible amounts are recommended, but no strict separation is needed. Lastly, the presence of S-based compounds (e.g., H_2S or SO_2) deactivates irreversibly the Ni-based catalyst; thus, purification of the inlet streams is mandatory to abate the sulfur content and preserve the catalytic activity.

4. Conclusions

A comprehensive study on the kinetic modeling and deactivation rates has been carried out on a 24 wt% Ni/Al_2O_3, suitable for converting both CO_2 and CO into CH_4. Firstly, the intrinsic kinetics and the corresponding kinetic parameters were obtained, considering an isothermal reactor, for Power-Law and LHHW-type kinetic expressions. On the one hand, Power-Law kinetic models provide a good description of the experimental datasets in which H_2/CO_2 and H_2/CO gas mixtures are individually fed to the reactor, but fail to describe the co-methanation of CO_2 and CO as the preferential CO adsorption is not considered. On the other hand, a careful study was conducted with LHHW-type kinetics, identifying the main reaction mechanisms.

Experimental evidence combined with literature information guided insights into the possibility that CO_2 methanation could occur on the Ni-based catalyst via either dissociative or H-assisted associative CO_2 adsorption forming CO* or COOH* species, respectively. The H_2 inhibition is related to a high H* coverage that favors the H-assisted hydrogenation of CO* into formyl (CHO*) and then its dissociation and hydrogenation into CH_x*. However, when CO is present in the gas mixture, its exergonic adsorption predominates and competes with the CO_2 adsorption. Thus, the excessive CO* coverage allows C* species to be produced; they can be hydrogenated into methane, form solid carbon on the surface, causing coking, or diffuse into the nickel structure forming nickel carbides. Among the different LHHW-type kinetic models, model M4 was able to describe all those aspects of the CO_2 and

CO methanation process by using a system of three reactions, minimizing the objective function and respecting the thermodynamic constraints.

Concerning the stability of the catalyst, long-term tests were performed under different reaction conditions and in presence of contaminants (C_2H_4 and O_2) or poisons (H_2S). Thermal sintering dominates during CO_2 methanation, but the catalyst exhibited a strong resistance; conversely, its stability dramatically decreased under CO methanation conditions due to the formation of nickel carbides at low temperatures ($T < 370$ °C), that reduce the CH_4 selectivity and produce several light hydrocarbons (from C_2 to C_5), and coking combined with thermal sintering at higher temperatures ($T > 370$ °C). However, during the CO_2 and CO co-methanation, the stability of the catalyst at low temperatures increased because no nickel carbides were produced, probably due to the slightly higher O* (or OH*) coverage. The presence of O_2 contaminations significantly affected the stability of the catalyst, while light olefins (such as C_2H_4) cause additional coking on its surface due to self-hydrogenation. Lastly, sulfur-based compounds (such as H_2S) are extremely dangerous for the catalyst because they deactivate it irreversibly under all circumstances. Power-Law deactivation rates were obtained to predict the catalyst stability under all those reaction conditions and allow the possibility of scaling up the CO_2 and CO methanation reactor.

CRediT authorship contribution statement

Fabrizio Celoria: Writing – review & editing, Writing – original draft, Visualization, Validation, Software, Investigation, Formal analysis, Data curation. **Fabio Salomone:** Writing – review & editing, Writing – original draft, Visualization, Validation, Software, Methodology, Investigation, Formal analysis, Data curation, Conceptualization. **Alessio Tauro:** Writing – review & editing, Writing – original draft, Visualization, Validation, Software, Investigation, Data curation. **Marta Gandiglio:** Writing – review & editing, Validation, Supervision, Resources, Methodology. **Domenico Ferrero:** Writing – review & editing, Validation, Supervision, Resources, Methodology. **Isabelle Champon:** Writing – review & editing, Validation, Software, Resources, Methodology. **Geneviève Geffraye:** Writing – review & editing, Validation, Supervision, Software, Resources, Methodology, Funding acquisition. **Raffaele Pirone:** Writing – review & editing, Supervision, Resources, Methodology, Conceptualization. **Samir Bensaid:** Writing – review & editing, Writing – original draft, Supervision, Resources, Project administration, Methodology, Funding acquisition, Conceptualization.

Declaration of competing interest

The authors declare that they have no known competing financial interests or personal relationships that could have appeared to influence the work reported in this paper.

Acknowledgements

The project leading to this research has received funding from the Horizon Europe research and innovation program under Grant Agreement No 101084288 (METHAREN Project). F.S. acknowledges the Italian Ministry of University and Research (MUR), program FSE REACT-EU PON Ricerca e Innovazione 2014-2020 (D.M. 1062/2021). A. T. acknowledges the PNRR program (DM 352/22) funded by the "Next Generation EU" program of the EU. The manuscript reflects the authors' views and opinions, neither the European Union nor the European Commission can be considered responsible for them. In addition, the authors acknowledge Enrico Sartoretti and Marco Allione for having performed SEM and TEM measurements, respectively.

Appendix A. Supplementary data

Supplementary data to this article can be found online at https://doi.org/10.1016/j.cej.2025.162113.

Data availability

Data will be made available on request.

References

[1] International Energy Agency, (2024). https://www.iea.org/world/energy-mix (accessed October 8, 2024).

[2] F. Salomone, E. Giglio, D. Ferrero, M. Santarelli, R. Pirone, S. Bensaid, Techno-economic modelling of a Power-to-Gas system based on SOEC electrolysis and CO_2 methanation in a RES-based electric grid, Chem. Eng. J. 377 (2019) 120233, https://doi.org/10.1016/j.cej.2018.10.170.

[3] E.A. Morosanu, A. Saldivia, M. Antonini, S. Bensaid, Process modeling of an innovative power to LNG demonstration plant, Energy Fuel 32 (2018) 8868–8879, https://doi.org/10.1021/acs.energyfuels.8b01078.

[4] E. Giglio, F.A. Deorsola, M. Gruber, S.R. Harth, E.A. Morosanu, D. Trimis, S. Bensaid, R. Pirone, Power-to-gas through high temperature electrolysis and carbon dioxide methanation: reactor design and process modeling, Ind. Eng. Chem. Res. 57 (2018) 4007–4018, https://doi.org/10.1021/acs.iecr.8b00477.

[5] A. Mazza, F. Salomone, F. Arrigo, S. Bensaid, E. Bompard, G. Chicco, Impact of Power-to-Gas on distribution systems with large renewable energy penetration, Energy Convers. Manage.: X 7 (2020) 100053, https://doi.org/10.1016/j.ecmx.2020.100053.

[6] F. Salomone, P. Marocco, D. Ferrario, A. Lanzini, D. Fino, S. Bensaid, M. Santarelli, Process simulation and energy analysis of synthetic natural gas production from water electrolysis and CO_2 capture in a waste incinerator, Appl. Energy 343 (2023) 121200, https://doi.org/10.1016/j.apenergy.2023.121200.

[7] I. Champon, A. Bengaouer, A. Chaise, S. Thomas, A.C. Roger, Carbon dioxide methanation kinetic model on a commercial Ni/Al_2O_3 catalyst, Journal of CO_2 Utilization 34 (2019) 256–265, https://doi.org/10.1016/j.jcou.2019.05.030.

[8] W. Wang, J. Gong, Methanation of carbon dioxide: an overview, Front. Chem. Eng. China 5 (2011) 2–10, https://doi.org/10.1007/s11705-010-0528-3.

[9] K. Stangeland, D. Kalai, H. Li, Z. Yu, CO_2 methanation: the effect of catalysts and reaction conditions, Energy Procedia 105 (2017) 2022–2027, https://doi.org/10.1016/j.egypro.2017.03.577.

[10] S. Ma, Y. Tan, Y. Han, Methanation of syngas over coral reef-like Ni/Al_2O_3 catalysts, J. Nat. Gas Chem. 20 (2011) 435–440, https://doi.org/10.1016/S1003-9953(10)60192-2.

[11] J.A. Onrubia-Calvo, A. Quindimil, A. Davó-Quiñonero, A. Bermejo-López, E. Bailón-García, B. Pereda-Ayo, D. Lozano-Castelló, J.A. González-Marcos, A. Bueno-López, J.R. González-Velasco, Kinetics, model discrimination, and parameters estimation of CO_2 methanation on highly active Ni/CeO_2 catalyst, Ind. Eng. Chem. Res. 61 (2022) 10419–10435, https://doi.org/10.1021/acs.iecr.2c00164.

[12] T.A. Le, M.S. Kim, S.H. Lee, T.W. Kim, E.D. Park, CO and CO_2 methanation over supported Ni catalysts, Catal. Today 293–294 (2017) 89–96, https://doi.org/10.1016/j.cattod.2016.12.036.

[13] S. Rönsch, J. Schneider, S. Matthischke, M. Schlüter, M. Götz, J. Lefebvre, P. Prabhakaran, S. Bajohr, Review on methanation - From fundamentals to current projects, Fuel 166 (2016) 276–296, https://doi.org/10.1016/j.fuel.2015.10.111.

[14] O. Mohan, S. Shambhawi, R. Xu, A.A. Lapkin, S.H. Mushrif, Investigating CO_2 methanation on Ni and Ru: DFT assisted microkinetic analysis, ChemCatChem 13 (2021) 2420–2433, https://doi.org/10.1002/cctc.202100073.

[15] T. Burger, P. Donaubauer, O. Hinrichsen, On the kinetics of the co-methanation of CO and CO_2 on a co-precipitated Ni-Al catalyst, Appl. Catal. B 282 (2021) 119408, https://doi.org/10.1016/j.apcatb.2020.119408.

[16] G.D. Weatherbee, C.H. Barthlomew, Hydrogenation of CO_2 on group VIII metals II. Kinetics and mechanism of CO_2 hydrogenation on nickel, J. Catal. 77 (1982) 460–472, https://doi.org/10.1016/0021-9517(82)90186-5.

[17] J. Xu, G.F. Froment, Methane steam reforming, methanation and water-gas shift: I. Intrinsic kinetics, AIChE J. 35 (1989) 88–96, https://doi.org/10.1002/aic.690350109.

[18] J. Kopyscinski, T.J. Schildhauer, F. Vogel, S.M.A. Biollaz, A. Wokaun, Applying spatially resolved concentration and temperature measurements in a catalytic plate reactor for the kinetic study of CO methanation, J. Catal. 271 (2010) 262–279, https://doi.org/10.1016/j.jcat.2010.02.008.

[19] R.P. Underwood, C.O. Bennett, The CO/H_2 reaction over nickel-alumina studied by the transient method, J. Catal. 86 (1984) 245–253, https://doi.org/10.1016/0021-9517(84)90370-1.

[20] F. Koschany, D. Schlereth, O. Hinrichsen, On the kinetics of the methanation of carbon dioxide on coprecipitated NiAl(O)x, Appl. Catal. B 181 (2016) 504–516, https://doi.org/10.1016/j.apcatb.2015.07.026.

[21] P. Marocco, E.A. Morosanu, E. Giglio, D. Ferrero, C. Mebrahtu, A. Lanzini, S. Abate, S. Bensaid, S. Perathoner, M. Santarelli, R. Pirone, G. Centi, CO_2 methanation over Ni/Al hydrotalcite-derived catalyst: experimental characterization and kinetic study, Fuel 225 (2018) 230–242, https://doi.org/10.1016/j.fuel.2018.03.137.

[22] E.A. Morosanu, F. Salomone, R. Pirone, S. Bensaid, Insights on a methanation catalyst aging process: aging characterization and kinetic study, Catalysts 10 (2020) 283, https://doi.org/10.3390/catal10030283.

[23] C. Wheeler, A. Jhalani, E.J. Klein, S. Tummala, L.D. Schmidt, The water–gas-shift reaction at short contact times, J. Catal. 223 (2004) 191–199, https://doi.org/10.1016/j.jcat.2004.01.002.

[24] D. Schmider, L. Maier, O. Deutschmann, Reaction kinetics of CO and CO_2 methanation over nickel, Ind. Eng. Chem. Res. 60 (2021) 5792–5805, https://doi.org/10.1021/acs.iecr.1c00389.

[25] A. Cárdenas-Arenas, A. Quindimil, A. Davó-Quiñonero, E. Bailón-García, D. Lozano-Castelló, U. De-La-Torre, B. Pereda-Ayo, J.A. González-Marcos, J. R. González-Velasco, A. Bueno-López, Isotopic and in situ DRIFTS study of the CO_2 methanation mechanism using Ni/CeO_2 and Ni/Al_2O_3 catalysts, Appl. Catal. B 265 (2020) 118538, https://doi.org/10.1016/j.apcatb.2019.118538.

[26] A. Quindimil, J.A. Onrubia-Calvo, A. Davó-Quiñonero, A. Bermejo-López, E. Bailón-García, B. Pereda-Ayo, D. Lozano-Castelló, J.A. González-Marcos, A. Bueno-López, J.R. González-Velasco, Intrinsic kinetics of CO_2 methanation on low-loaded Ni/Al_2O_3 catalyst: mechanism, model discrimination and parameter estimation, J. CO_2 Util. 57 (2022) 101888, https://doi.org/10.1016/j.jcou.2022.101888.

[27] P. Strucks, L. Failing, S. Kaluza, A short review on Ni-catalyzed methanation of CO_2: reaction mechanism, catalyst deactivation, dynamic operation, Chem. Ing. Tech. 93 (2021) 1526–1536, https://doi.org/10.1002/cite.202100049.

[28] J.R. Rostrup-Nielsen, K. Pedersen, J. Sehested, High temperature methanation Sintering and structure sensitivity, Appl. Catal. A Gen. 330 (2007) 134–138, https://doi.org/10.1016/j.apcata.2007.07.015.

[29] I. Champon, A. Bengaouer, A. Chaise, S. Thomas, A.-C. Roger, Modelling the sintering of nickel particles supported on γ-alumina under hydrothermal conditions, Catalysts 10 (2020) 1477, https://doi.org/10.3390/catal10121477.

[30] S. Ewald, M. Kolbeck, T. Kratky, M. Wolf, O. Hinrichsen, On the deactivation of Ni-Al catalysts in CO_2 methanation, Appl. Catal. A Gen. 570 (2019) 376–386, https://doi.org/10.1016/J.APCATA.2018.10.033.

[31] S. Abelló, C. Berrueco, D. Montané, High-loaded nickel–alumina catalyst for direct CO_2 hydrogenation into synthetic natural gas (SNG), Fuel 113 (2013) 598–609, https://doi.org/10.1016/j.fuel.2013.06.012.

[32] G. Garbarino, P. Riani, L. Magistri, G. Busca, A study of the methanation of carbon dioxide on Ni/Al_2O_3 catalysts at atmospheric pressure, Int. J. Hydrogen Energy 39 (2014) 11557–11565, https://doi.org/10.1016/j.ijhydene.2014.05.111.

[33] M. Wolf, C. Schüler, O. Hinrichsen, Sulfur poisoning of co-precipitated Ni–Al catalysts for the methanation of CO_2, J. CO_2 Util. 32 (2019) 80–91, https://doi.org/10.1016/j.jcou.2019.03.003.

[34] E. Rozzi, F.D. Minuto, A. Lanzini, P. Leone, Green synthetic fuels: renewable routes for the conversion of non-fossil feedstocks into gaseous fuels and their end uses, Energies (Basel) 13 (2020), https://doi.org/10.3390/en13020420.

[35] F. Santoni, P. Gislon, E. Rozzi, M. Gandiglio, S. McPhail, A. Lanzini, M. Pagani, S. Fiorilli, Hydrogen sulphide and carbonyl sulphide removal from biogas for exploitation in high-temperature fuel cells, Waste Biomass Valorization 15 (2024) 577–597, https://doi.org/10.1007/s12649-023-02212-6.

[36] F. Salomone, E. Sartoretti, S. Ballauri, M. Castellino, C. Novara, F. Giorgis, R. Pirone, S. Bensaid, CO_2 hydrogenation to methanol over Zr- and Ce-doped indium oxide, Catal. Today 423 (2023) 114023, https://doi.org/10.1016/j.cattod.2023.01.030.

[37] B.R. Bird, W.E. Stewart, E.N. Lightfoot, Transport Phenomena, 2^{nd} ed, John Wiley & Sons, New York, 2002. Doi:10.1007/s007690000247.

[38] NIST Chemistry WebBook, (n.d.). https://webbook.nist.gov/chemistry/ (accessed October 24, 2024).

[39] D. Schlereth, O. Hinrichsen, A fixed-bed reactor modeling study on the methanation of CO_2, Chem. Eng. Res. Des. 92 (2014) 702–712, https://doi.org/10.1016/j.cherd.2013.11.014.

[40] B.E. Poling, J.M. Prausnitz, J.P. O'Connell, The Properties of gases and liquids, 5th ed., McGraw-Hill Inc, 2000.

[41] D.C. Montgomery, Design and Analysis of Experiments, 8th ed., John Wiley & Sons Inc, 2013.

[42] T. Van Herwijnen, H. Van Doesburg, W.A. De Jong, Kinetics of the methanation of CO and CO_2 on a nickel catalyst, J. Catal. 28 (1973) 391–402, https://doi.org/10.1016/0021-9517(73)90132-2.

[43] J. Sehested, S. Dahl, J. Jacobsen, J.R. Rostrup-Nielsen, Methanation of CO over nickel: mechanism and kinetics at high H_2/CO ratios, J Phys Chem B 109 (2005) 2432–2438, https://doi.org/10.1021/jp040239s.

[44] Y. Leng, H. Shao, Y. Wang, M. Suzuki, X. Li, A new method to synthesize nickel carbide (Ni_3C) nanoparticles in solution, J. Nanosci. Nanotechnol. 6 (2006) 221–226, https://doi.org/10.1166/jnn.2006.17934.